Bachelor Project

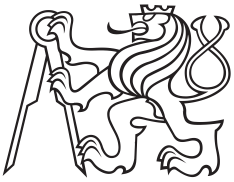

Czech Technical University in Prague

F4

Faculty of Nuclear Sciences and Physical Engineering
Department of Physics

Study of the B_s meson properties at the ATLAS detector at the LHC

Zbyněk Nguyen

Supervisor: Ing. Tomáš Jakoubek
Field of study: Nuclear Engineering
Subfield: Experimental Nuclear Physics
July 2015

Bakalářská práce

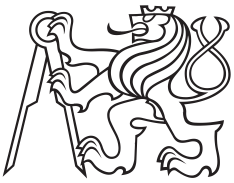

České
vysoké
učení technické
v Praze

F4

Fakulta jaderná a fyzikálně inženýrská
Katedra fyziky

Studium vlastností B_s mezonu na experimentu ATLAS na LHC

Zbyněk Nguyen

Vedoucí: Ing. Tomáš Jakoubek
Obor: Jaderné inženýrství
Studijní program: Experimentální jaderná fyzika
Červenec 2015

Acknowledgements

My profound thanks go to my thesis supervisor for introducing me to the field of B-physics and for his friendly approach, valuable discussions and patience. I am very grateful to A. Květoň, E. Davídková and G. Bhalla for providing language corrections. Special thanks go to my family and friends for their encouragement and support.

Declaration

I hereby declare that this thesis is my own work and I have properly cited all sources used in the thesis.

I agree on the usage of this thesis in compliance with the Copyright Act.

Prague, 22nd July 2015

.....
Zbyněk Nguyen

Abstract

B_s meson is a bound state of a bottom antiquark and a strange quark. Thanks to flavour-changing weak decays of the constituent quarks, the B_s meson is able to spontaneously transform into its own antiparticle $\bar{B}_s$. This is of interest in particle physics but also in other fields such as cosmology. Aim of this work is to familiarize oneself with the particle physics, especially the study of beauty particles and their decays, the ATLAS detector at the LHC, and computer-based analysis of large datasets. The unbinned maximum likelihood fit will be performed to extract the two properties of the B_s meson – its mass and lifetime.

Keywords: B-physics, ATLAS, LHC, fitting, unbinned likelihood

Supervisor: Ing. Tomáš Jakoubek

Abstrakt

B_s meson je vázaný stav antikvarku $\bar{b}$ a kvarku s. Vzhledem k tomu, že slabá interakce je schopna měnit vůni obou kvarků, je B_s meson schopen spontánní přeměny na svou antičástici $\bar{B}_s$. Tento proces je zajímavý nejen pro částicovou fyziku, nýbrž v konečném důsledku i pro kosmologii. Cílem této práce je seznámit se s částicovou fyzikou, zejména se studiem půvabných mesonů a jejich rozpady, dále se s detektorem ATLAS na urychlovači LHC a s počítačovým zpracováním velkých objemů dat. K získání dvou klíčových vlastností B_s mesonu, hmotnosti a doby života, použijeme fitování tzv. „nebinovanou věrohodnostní funkcí“ (častěji je však používán anglický název).

Klíčová slova: B-fyzika, ATLAS, LHC, fitování, nebinovaná věrohodnostní funkce

Překlad názvu: Studium vlastností B_s mezonu na experimentu ATLAS na LHC

Contents

Figures

Tables

Introduction

The last century drastically changed our view on the world around us. Technological advancements went hand in hand with theoretical development, allowing us to see deeper into the structure of matter. Every once in a while we seemingly reached a limit in the understanding of things, but always, a surprising discovery emerged later, shedding light on some new physics.

For instance, an observation of an effect called the CP violation in 1964 and the subsequent beauty quark discovery sparked enough interest in the high-energy physics community so that a new branch of physics was born, devoted entirely to investigation of these new beauty particles – now known as B mesons – and their properties. The B mesons with no electric charge (B_s and B_d) have some remarkable properties, such as that they can transform into their own antiparticle and vice versa.

The object of this thesis is the study of these particles. It is inspired by the ATLAS article [10], where mass as well as lifetime of the B_s meson were extracted from the 2010 data at $\sqrt{s} = 7$ TeV, using unbinned maximum likelihood fit. Analysis in this work will be performed on the newer 2012 data at $\sqrt{s} = 8$ TeV and it will serve as a basis for a more thorough analysis.

The thesis is structured as follows. In the first chapter, we provide an introduction to the theoretical framework. Then, beauty mesons are briefly introduced. In the second chapter, we characterise several collider-related variables and describe the ATLAS detector. In Chapter 3, we focus on the B-physics and CP violation. In the penultimate chapter, we prepare the data analysis and describe the data selection, and in the final chapter, results are presented.

Chapter 1

Theoretical introduction

1.1 Symmetries

An important property of science is the ability to abstract and extrapolate; decide which effects are insignificant for a phenomenon and neglect them. One of key concepts that provides this ability is *symmetry*. An object is said to be symmetric (or invariant) with respect to a certain transformation if it stays unchanged after applying the transformation.

In classical mechanics, the dynamics of a system are determined from a Lagrangian by the means of equations of motion. As solving two Lagrangians may yield the same equations of motion, the Lagrangian is not uniquely given. By Noether's theorems, for every symmetry[1] of a Lagrangian there exists a conserved quantity called the constant of motion. This is where the symmetry enters the field of physics – as an attribute of the system.

The underlying properties of space and time yield basic continuous symmetries, which in turn result in fundamental conserved quantities.

property	symmetry	conserved quantity
homogeneity of space	translation	total linear momentum
homogeneity of time	time shift	total energy
isotropy of space	rotation	total angular momentum

Table 1.1: Conservation laws resulting from the properties of space and time.

The mathematical framework of particle physics – the Standard Model – is built in reverse. Given a system with specific symmetries[2], we are to find the most general Lagrangian on which the invariance to these symmetries is imposed. Called local gauge symmetries, they establish the existence of degrees of freedom not corresponding to changes in physical state.

Symmetries are closely related to groups (mathematical structures closed under products and inverses), and so the language of modern particle physics is mainly group-theoretic. This was pioneered by Eugene P. Wigner in the

[1] Global and continuous.
[2] Local and continuous.

late 1930s, who introduced the study of groups to particle physics. He did so by linking particles to representations of the group of space-time symmetries. In this fashion, symmetries are represented by groups, and groups generate mediating particles, which are called gauge bosons.

1.1.1 Discrete symmetries

In quantum mechanics, the state of a particle a corresponds to the ket $|a\rangle$ (see Appendix A for notation) which satisfies the equation of motion. In the non-relativistic spinless case, that is the time-dependent Schrödinger equation

$$\mathrm{i}\frac{\partial}{\partial t}|a\rangle = \hat{\mathrm{H}}\,|a\rangle\,. \tag{1.1}$$

Observables, such as the Hamiltonian $\hat{\mathrm{H}}$ above, are represented by self-adjoint operators on the Hilbert space $\mathcal{H}$, which are acting on these vectors. This guarantees the expectation values (measurable quantities) $\langle a|\hat{\mathrm{O}}|a\rangle$ are real. Symmetries are represented by (anti-)unitary operators. This causes their eigenvalues to have a magnitude of 1. There are three discrete space-time symmetries.

- The charge conjugation operator $\hat{\mathrm{C}}$ replaces particle a with its own antiparticle $\bar{a}$: $\hat{\mathrm{C}}\,|a\rangle = C\,|\bar{a}\rangle$. As antiparticles and particles share same lifetimes τ and masses m, but differ in the sign of electric charge q and magnetic moment $\boldsymbol{\mu}$, the $\hat{\mathrm{C}}$ operator reverses the sign of the latter two quantities.
- The parity inversion operator $\hat{\mathrm{P}}$ mirrors the position vector $\boldsymbol{r}$. Let $\psi_a(\boldsymbol{r},t)$ denote the ket $|a\rangle$ in the position basis, the operator is then defined as $\hat{\mathrm{P}}\psi_a(\boldsymbol{r},t) = P\psi_a(-\boldsymbol{r},t)$.
- The time reversal operator $\hat{\mathrm{T}}$ changes the time reading: $\hat{\mathrm{T}}\psi_a(\boldsymbol{r},t) = T\psi_a(\boldsymbol{r},-t)$.

The eigenvalues C, P and T of these operators are all of value ± 1. We can accordingly assign the C, P and T values to particles and call, for instance, C-odd those with $C = -1$, and C-even those with $C = -1$; same with the remaining symmetries. For a composite system, the eigenvalues a product of the constituent particles.

1.2 Observables

1.2.1 Spin

Spin is an internal degree of freedom first proposed by W. Pauli in 1920s. Spin emerges in quantum mechanics from the behaviour of wavefunctions (with multiple components) under rotations. The resulting representation of

a particle can be factorised as $|a\rangle = |\psi\rangle \otimes |\chi\rangle$, into the space part $|\psi\rangle$ and the multi-component part $|\chi\rangle$ called a spinor.

Spin is in general a vector-like quantity and its corresponding operator $\hat{\mathbf{S}}$ is a vector operator. However, instead of spin „vectors“ themselves, their magnitude S and projection S_3 into the z-axis are used. Both are commonly referred to as spin. The projection S_3 can assume one of $2S + 1$ values: $-S, -S + 1 \ldots, S - 1, S$.

Both S and S_3 are measured in rational multiples of $\hbar$, just like the classical angular momentum. Particles, elementary or composite, are split into two types according to their S.

Bosons are characterized by having integer spin. Their distribution is given by Bose-Einstein statistics, after which they are named. The Pauli exclusion principle does not apply, i.e., two bosons can occupy the same quantum state. Their wavefunction is symmetric.

Fermions are characterized by having half-integer spin. Their distribution is given by Fermi-Dirac statistics, after which they are named. They are subject to the Pauli exclusion principle, therefore two fermions cannot occupy the same quantum state. Their wavefunction is asymmetric.

Particle spin and its parity P are often written simultaneously in the J^P formalism, where J is the sum of the spin (S) and angular (L) momenta, $J = L + S$. We say that a particle is either a scalar (0^+), pseudoscalar (0^-), vector (1^-), axial vector (1^+) or a tensor (2^+).

1.2.2 Helicity and chirality

Spin is defined in a reference frame dependent way – in principle, the choice of the z-axis is arbitrary. This can be avoided using the helicity variable λ, which does not depend on the choice of an external axis. Instead, it projects spin S into the direction of movement. The helicity operator is thus defined as

$$\hat{\lambda} = \frac{\hat{\mathbf{S}} \cdot \hat{\mathbf{p}}}{\|\hat{\mathbf{p}}\|}, \tag{1.2}$$

as a scalar product of the spin $\hat{\mathbf{S}}$ and the unit momentum operator $\hat{\mathbf{p}}/\|\hat{\mathbf{p}}\|$. The eigenvalues of helicity range from $-S, -S + 1 \ldots, S - 1, S$ as well. The positive values correspond to the spin pointing in the same direction as the momentum and negative for the opposite direction. For a massless particle, only the lateral values are permitted: $-S, S$.

Helicity and momentum operators commute hence they can be measured simultaneously. Clearly, we can label states either with their spin or helicity, as helicity states form a different, yet complete basis. Helicity is also a Lorentz-invariant quantity.

Chirality, another quantum mechanical quantity, is a related concept to helicity. It can divide particles into left- and right-handed based on their behaviour under Lorentz transformation. A similar analogy can be found

in how left and right hand behave under rotations in a plane – one cannot be rotated into another. Despite that, it is a mathematical concept rather than a physical one like helicity, which is important for the study of weak interactions. For a massless particle, the chirality coincides with helicity.

1.3 Standard Model

The Standard Model of particle physics (SM) is a theory concerning all known subatomic particles and interactions between them. Formed in the early 1970s, it has proven to be very successful. Not only it withstood thorough experimental testing, but it also predicted a number of new particles – the latest one being the Higgs boson, discovered in 2012.

The particle content of the Standard Model can be summarized by the following sentence:

> All matter with which we came in contact with is made of 6 leptons and 6 quarks and interactions among those are mediated through 4 gauge bosons, with the Higgs boson explaining the symmetry breaking.

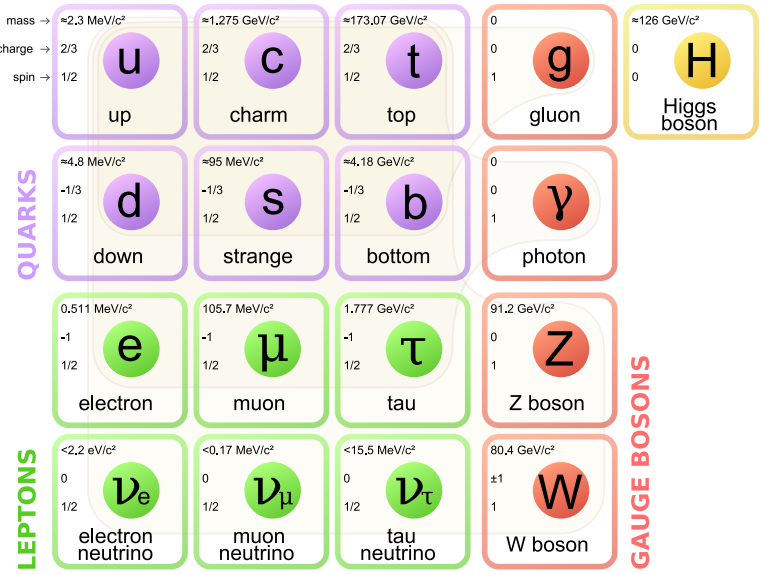

Fig. 1.1: Table of elementary particles in the Standard Model. [1]

All in all, there are 17 *types* of particles. An antiparticle exists for each elementary fermion. Moreover, there are 3 quarks per quark type, and 8 gluons, which leads to a total number of 61 elementary particles and antiparticles: 6×2 (anti-)leptons, $6 \times 2 \times 3$ (anti-)quarks, 8 gluons, 4 gauge bosons and 1 Higgs boson.

1.4 Matter particles

There are two types of matter particles – quarks and leptons – and they can be split into three families, or generations.

1.4.1 Leptons

Leptons are fermions carrying negative or zero electric charge in units of e.

The first known lepton was the electron, hypothesised and observed far earlier than other elementary particles. This can be attributed to the electron shell, the outermost layer of the atom, being responsible for the atomic properties.

Later, more types of leptons have been observed and classified. There are three electrically charged leptons with charge of $-e$ and for each one, there is a corresponding neutral lepton called a neutrino. We call these pairs generations and write them as doublets

$$\begin{pmatrix} \nu_e \\ e^- \end{pmatrix}, \begin{pmatrix} \nu_\mu \\ \mu^- \end{pmatrix}, \begin{pmatrix} \nu_\tau \\ \tau^- \end{pmatrix}. \tag{1.3}$$

Each generation is characterised by its own lepton number: L_e, L_μ and L_τ. The lepton number is conserved, photons can therefore create an electron-positron pair (e^+e^-) but not e^-e^- pair; and in beta decay, antineutrino $\bar{\nu}_e$ must be created to balance the electron.

The electron is the lightest charged lepton. Compared to the proton, it is approximately 1800 times lighter, and does not add significant weight to an atom. It has been indirectly observed in the form of electricity through phenomena such as lightning and static electricity between fur and amber („elektron“ in a Greek word for amber). Later, electricity has been harnessed as a means to store and transfer energy. Discovery of the electron by J.J. Thomson on the verge of the 19th century catalysed the study of its particle and wavelike properties. Electrons suffer from massive radiative losses when decelerated. This is called the deceleration radiation (bremsstrahlung).

The muon is approximately 207 times heavier than the electron, with other properties being identical. This makes muons less prone to bremsstrahlung, enabling them to penetrate matter deeply. On Earth, they originate as the by-product of the cosmic radiation, and due to their high mass and relativistic speed (hence, time dilatation), such muons can even penetrate the ground or sea level.

The tauon is the heaviest lepton, potentially even more penetrating than muon. On the other hand, their short lifetime prevents tauons from existing in a bound state. Due to their high mass, they are the only leptons capable of hadronic decay.

Neutrinos are chargeless and near-massless particles. This makes them extremely difficult to detect as they do not interact electromagnetically nor strongly, and so they pass through Earth unnoticed. The majority of these are produced in the Sun through nuclear fusion. The first neutrino ν_e was proposed in the early 20th century as the means to explain the apparent violation of energy and momentum conservation in beta decay. As an interesting remark, only left-handed neutrinos and right-handed antineutrinos have been observed. By handedness, chirality is meant, i.e. negative (left-handed) or positive (right-handed) helicity.

1.4.2 Quarks

Quarks are fermions carrying electric charge of fractional multiples of e. In addition, they carry a new degree of freedom called colour charge, which will be discussed later. There are 6 flavours of quarks which can be translated to 5 quantum numbers: isospin projection I_3, strangeness S, charm C, beauty B' and truth T.

The nucleus of the atom was thought to be composed of indivisible particles called nucleons. New particles were later discovered in cosmic rays (and later, in collider experiments), bearing similar properties, such as interacting via the strong interaction. A new theory, capable of organizing this excessive particle zoo, arose in the 1960s, with a surprising solution. These newly observed particles, hadrons, as we call them today, could be understood as bound states of some elementary particles called quarks.

Quarks are only observed in these bounded states called hadrons.

Baryons – made of 3 quarks ($q_i q_j q_k$) or 3 antiquarks ($\bar{q}_i \bar{q}_j \bar{q}_k$).

Mesons – made of a quark-antiquark pair ($\bar{q}_l q_m$).

Other types of hadrons are hypothesised, such as tetraquarks, pentaquarks or dibaryons, but their existence is not fully confirmed yet. A tetraquark candidate has been observed in 2014 [11], and pentaquark candidate has been observed just recently [12] (a not yet reviewed report). Nonetheless, these exotic hadrons do not fit the usual quark model.

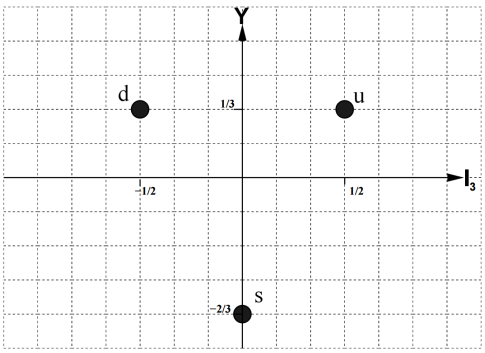

Fig. 1.2: Weight diagram for light quark triplet. [2]

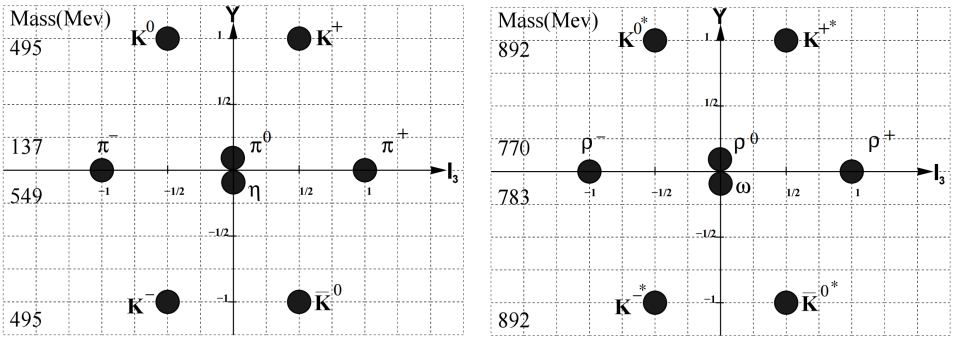

(a) : Octet **(b) :** Singlet

Fig. 1.3: Weight diagrams for strange mesons. [2]

The first quark model was introduced by M. Gell-Mann and independently by G. Zweig in 1964 and based on the $SU(3)$ symmetry. A third quark, called strange (s), was added to the known quarks, up (u) and down (d). However, due to their inequal masses, the $SU(3)$ symmetry is slightly broken. The quark triplet can be plotted in the (I_3, Y) plane, as shown in Fig. 1.2, with Y being the hypercharge defined in Eq. (1.4). Such graphs are called weight diagrams.

Applying product rules for groups, one can acquire weight diagrams for composite particles, as shown on Fig. 1.3 in case of mesons.

A fourth quark was speculated and confirmed to exist later, called the charm quark (c), which gave further confidence in the quark model. Subsequently, another generation of quarks was discovered, the bottom (b), and top (t). Quantum numbers C, B', and T were assigned to these new quarks, respectively.

Additionally, baryon number B is defined roughly to be $B = 1$ for baryons, $B = -1$ for antibaryons and $B = 0$ for mesons. All quark numbers satisfy the famous Gell-Mann–Nishijima formula

$$Q = I_3 + \frac{1}{2}\underbrace{(B + S + C + B' + T)}_{Y}, \tag{1.4}$$

where Q is the electric charge and Y the hypercharge.

It is possible to extend the $SU(3)$ symmetry to include these new quark quantum numbers. For instance, adding the beauty number B' yields $SU(4)$ symmetry. The mass difference is even more prevalent due to b quark being significantly heavier than the rest of the triplet, and so the symmetry is even more broken. The resulting weight diagram is plotted in the $(I_3, Y, -B')$ space on Fig. 1.4 and it now incorporates mesons with non-zero beauty called B mesons.

An analogous procedure can be applied with charm number C instead of beauty so that mesons with non-zero charm can be plotted. These are called D mesons. Combining both beauty and charm numbers into the weight diagram would result in a badly broken $SU(5)$ symmetry which would be

difficult to plot. As top quark doesn't produce composite particles, adding truth T to the (I_3, Y) plane is of no use.

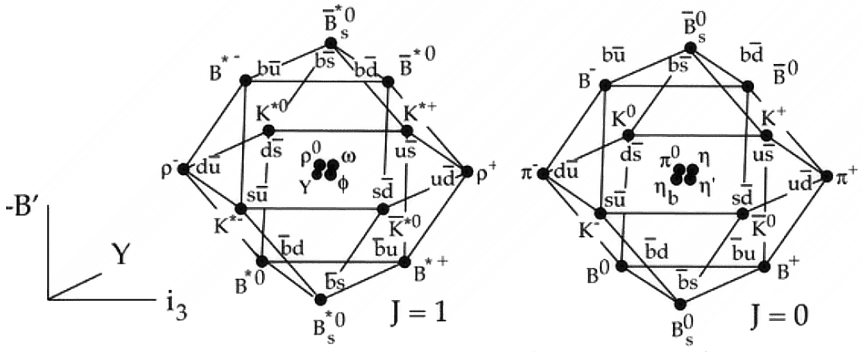

Fig. 1.4: Weight diagrams for beauty mesons. [3]

Due to this significant difference between masses of uds and cbt quarks, the latter are called heavy. The field of physics devoted to the study of B and D mesons is accordingly called heavy flavour physics, and in special case of B mesons, B-physics.

Among the heavy flavour hadrons, the ones with hidden[3] beauty and charm are especially notable. They are called charmonia ($c\bar{c}$) or bottomonia ($b\bar{b}$), made out of quark-antiquark pairs. The lowest excited state of charmonium $c\bar{c}$ is known as the J/ψ meson.

1.5 Interactions

There are four commonly accepted fundamental interactions. Whereas the model of the gravitational interaction is a classical field theory, the remaining three – electromagnetic, weak and strong – are quantized, meaning that the interaction is performed via a particle exchange.

	strong	electromagnetic	weak	gravitational
charge	colour	electric	flavour	energy/mass
acts on	quarks, gluons	elect. charged	quarks, leptons	all
coupling const.	$\alpha_S \approx 1$	$\alpha \approx 1/137$	$\alpha_W \approx 10^{-6}$	$\alpha_G \approx 10^{-39}$
range [m]	10^{-15}	∞	10^{-18}	∞
symmetry	$SU(3)$	$SU(2) \times U(1)$		?
gauge boson	gluons g_i	photon γ	$W^{\pm}$, Z^0	graviton?
mass [MeV]	0	0	$\approx 80, 90$	0?
J^P	1^-	1^-	1^-	2?

Table 1.2: Overview of the fundamental interactions.

[3] The total charm of $c\bar{c}$ cancels out but the constituents are not charmless, similar with $b\bar{b}$.

1.5.1 Electromagnetic

As the name suggests, the electromagnetic interaction is responsible for all electric, magnetic and related phenomena. Not only that – due to its nature, it is the cause of virtually all phenomena happening outside the nucleus, namely, chemical bonds and electrostatic repulsion.

First developed as a classical field theory thanks to J.C. Maxwell in the 1860s, it was then extended to incorporate relativistic effects, combined with quantum mechanics and reformulated in terms of quantum field theory, called quantum electrodynamics (QED). This was the first successful quantum field theory, successfully predicting several physical quantities. The common approach to QED is perturbative.

The electromagnetic interaction acts on particles of non-zero electric charge. It has infinite range and obeys the inverse square law. It can be both attractive or repulsive.

The electromagnetic field is symmetric against a change of a complex phase, which corresponds to the $U(1)$ symmetry. By the Noether's theorems, this yields the conservation of electric charge. The mediating boson is called the photon (γ). It is massless due to the infinite range of the interaction, and it is a vector boson.

1.5.2 Weak

Weak interaction causes radioactive beta decays. This consequently allows applications like carbon dating. It also plays a pivotal role in nuclear fusion (specifically, deuteron production), that can be harnessed on Earth as a source of energy in devices such as tokamaks.

It was proposed by E. Fermi in the 1930s as means to explain the beta decay. It was resolved by the existence of the neutrino, an undetectable particle, seemingly not interacting at all, or if it was, then very *weakly*. Hence, the name weak interaction. Sadly, Fermi interaction was not renormalizable[4]. That was possible only after unifying the weak interaction with electromagnetism, creating the electroweak theory (EWT), based on the symmetry of $SU(2) \times U(1)$.

Weak interaction acts on particles with flavour, which is a property of quarks and leptons, but is inherited by the composite particles of these. The weak interaction is unique in the aspect that it can even change the flavour of the particle, and as a result, change the particle itself. It is also the only fundamental interaction which does not produce bound states.

There are three mediating bosons, called $W^{\pm}$ and Z^0, which, unlike other gauge bosons, have significant masses. This causes the short lifetime of these particles and short range of the interaction. The name W stands for weak, whereas Z stands for zero electric charge, and all of them are vector bosons. The Standard Model suggests that their masses come from the effect of the Higgs field, which is represented by the Higgs boson.

[4] In the study of quantum field theories, infinities in can arise. Techniques collectively called renormalization are a way how to treat and remove these infinities.

1.5.3 Strong

The strong interaction secures the stability of matter by binding the particles into the minute volume of the nucleus, overcoming enormous repulsion therein. It is by far the strongest of all interactions. The need for strong interaction emerged from deep inelastic scattering of a proton, revealing an internal structure. A parton model was proposed, but later it became clear that partons correspond to quarks and particles now referred as gluons.

The interaction acts on all colour-charged particles. Colour is a new degree of freedom that is associated with quarks only. It was introduced so that Pauli exclusion principle is not compromised in case of a particle such as Δ^{++} (uuu), which would otherwise consist of same-state fermions. There are three colours, denoted with as red, green, blue (rgb), and their anticolours $(\bar{r}\bar{g}\bar{b})$, which add in accordance to their real world counterparts. Only colourless (white) combinations of quarks are observed, hence the need to create bounds states. Accordingly, baryons are composed from either (rgb) or $(\bar{r}\bar{g}\bar{b})$, and mesons take the form of an colour-anticolour quark pair.

The three colours correspond to the symmetry $SU(3)$. There are 8 mediating bosons called gluons, each gluon binding to different colour combinations. Therefore, gluons themselves carry colour (a property unlike other gauge bosons) and in consequence, are responsible for colour changes in quarks. It also means that gluons can interact with each other, leading to gluon anti-screening and rendering the perturbative approach to QCD impossible.

1.5.4 Gravitational

Several properties set the gravitational interaction apart from the others. It is the only interaction acting on all particles of non-zero energy, but at the same time, it is by far the weakest. Most importantly, it is the primary means of interaction in the cosmological scale because of its long-range character. It always acts as an attractive force. Similarly to electromagnetism, it obeys the inverse square law.

Gravitational interaction is not covered by the Standard Model. It is described by A. Einstein's General theory of relativity. Should gravity have a mediating gauge boson, it would be a massless tensor boson (spin 2) of no charge, a hypothesised particle called graviton. Existence of such particle is yet to be experimentally confirmed.

Fortunately, at subatomic scale, the effect of the gravitational interaction is negligible.

1.6 Beyond the Standard Model

Even though the Standard Model is one of the greatest achievements of theoretical physics, it cannot be considered an ultimate theory, as there are certain questions that cannot be answered within the current Standard Model.

Philosophical questions

The Standard Model depends on 19 arbitrary parameters, whose numerical values cannot be determined theoretically – they have to be determined experimentally.

Furthermore, there are three generations of fermions, and apparently can be only three. Is there a specific reason for this?

Neutrino physics

Neutrinos are assumed to be extremely light, but not massless. Their masses would be additional parameters in the Standard Model.

Right-handed neutrinos are also yet to be found. A non-massless theory would require them to exist.

Cosmology

There have not been successful attempts of quantizing gravity as the resulting theory was not renormalizable. The gravitational interaction thus remains incompatible with the Standard Model. Additionally, there is no reason for gravity to be that weak by contrast to other interactions. This is called the hierarchy problem.

Dark matter, a hypothetical kind of matter, appears to be the main matter constituent of the universe. Dark energy is hypothesised to pervade the Universe, causing its expansion. There are almost no predictions for either dark matter or energy.

Another fact is the baryon asymmetry. After the Big Bang, an equal amount of matter and antimatter should have been produced, yet nowadays, antimatter practically does not exist. We do not know what caused this imbalance, but a possible solution might be the CP violation (Section 3.2.3).

1.6.1 New theories

Electroweak theory is not yet unified with strong interaction. A theory that would unify all three Standard Model interactions is called Grand Unified Theory (GUT). Meanwhile, there are several attempts at quantum gravity (QG) undergoing. If one was to merge QG and GUT, the resulting Theory of Everything (TOE) would be the ultimate theory of all four interactions.

Chapter 2

ATLAS experiment

2.1 High energy physics

The aim of the contemporary experimental particle physics is to study and test processes that are predicted by the theory, and possibly find new phenomena beyond the Standard Model. To make this possible, scientific facilities have been built, containing high-precision equipment of severe complexity, such as particle accelerators.

These devices are capable of studying processes at a scale delicate enough to „see“ the fundamental particles. For that, a probing particle is accelerated to high energies. In analogy to optical microscopes, studying objects with certain precision requires the probing particle to have a wavelength of same or smaller magnitude. As energy is inversely proportional to wavelength by the formula $E = h/\lambda$, to achieve a shorter wavelength, a higher energy is needed.

As our technology was getting more precise, we were able to see deeper into the structure of atomic particles, rendering some of them no longer fundamental, revealing their inner structure.

Additionally, by the mass-energy equivalence $E = mc^2$, collision energy is spent for new particle production. Since many predicted particles are very massive, bigger accelerators were needed to be able to produce these particles. The search is still on and new particles (supersymmetric partners, gravitons and such) can be discovered.

Finally, at exceedingly high energy densities, constituents of baryonic matter (quarks and gluons) become deconfined, allowing a state of matter known as quark-gluon plasma (QGP). This study is of high cosmological interest, as quark-gluon plasma is believed to be the state of the Universe directly after the Big Bang. This also allows for the study of the properties of the strong interaction.

For the reasons outlined above, the meanings of ‘particle physics’ and ‘high energy physics’ (HEP) often coincide, and particle accelerators are built for the purpose of studying particle physics, with more advanced accelerators planned in the future. As a by-product, high energy physics research can result in inventions utilized commonly today, such as PET/CT scans, or the World Wide Web.

2.2 Collider variables

In particle accelerators, particles, such as protons, are accelerated and collided. Due to the proton size, it is improbable that individual protons would collide. Instead, localized streams of particles are accelerated, called beams. Beams are not homogeneous streams of energy – they contain spaced packages called bunches.

2.2.1 Collision energy

There are two ways to perform a collider experiment. Either a beam is aimed at a stationary target, or two beams are collided against each other. Calculation of the energy of the collision for both types will follow.

The four-momentum P^ν for a particle with energy E and momentum $\boldsymbol{p}$ is given by

$$P^\nu = \begin{pmatrix} E \\ \boldsymbol{p} \end{pmatrix}. \tag{2.1}$$

Its Minkowski norm is the same in all reference frames, hence called invariant mass m_0^2.

$$P^\nu P_\nu = E^2 - \|\boldsymbol{p}\|^2 = m_0^2. \tag{2.2}$$

In the ultra-relativistic limit ($E \gg m_0^2$), the magnitude of energy is approximately the same as the one of momentum, $E \approx p$.

Given a fixed-target experiment, the four-momenta P_1^ν of incoming particle and P_2^ν of the target particle are

$$P_1^\nu = \begin{pmatrix} E_1 \\ \boldsymbol{p} \end{pmatrix}, \quad P_2^\nu = \begin{pmatrix} m_0 \\ \boldsymbol{0} \end{pmatrix}, \tag{2.3}$$

assuming both particles have same mass m_0. The norm of $P = P_1 + P_2$ gives the energy of collision E_{CM} in the centre-of-mass frame,

$$P^\nu P_\nu = 2m_0^2 + 2m_0^2 E_1 = E_{\mathrm{CM}}^2, \tag{2.4}$$

where the Eq. (2.2) was used for both P_1 and P_2. In the ultra-relativistic limit,

$$E_{\mathrm{CM}} \approx \sqrt{E_1}. \tag{2.5}$$

In a colliding beam experiment, the four-momenta P_1^ν and P_2^ν of both beams are

$$P_1^\nu = \begin{pmatrix} E_1 \\ \boldsymbol{p}_1 \end{pmatrix}, \quad P_2^\nu = \begin{pmatrix} E_2 \\ \boldsymbol{p}_2 \end{pmatrix}, \tag{2.6}$$

and the norm of $P = P_1 + P_2$ gives

$$P^\nu P_\nu = (E_1 + E_2)^2 - (\boldsymbol{p}_1 + \boldsymbol{p}_2)^2 = E_{\mathrm{CM}}^2. \tag{2.7}$$

Thanks to the beams heading in opposite directions, the momenta $\boldsymbol{p}_2$ and $\boldsymbol{p}_1$ will cancel out and the remaining terms give the E_{CM} as

$$E_{\mathrm{CM}} = E_1 + E_2. \tag{2.8}$$

Comparing Eq. (2.8) and Eq. (2.5) shows a higher possible energy in favour of the colliding beam experiment. Another advantage is that the collision point lies in the laboratory rest frame. Using Mandelstam variables, the energy in the centre-of-mass frame is often denoted as $\sqrt{s} = E_{\mathrm{CM}}$. It is a crucial collider parameter as it is directly related to particle production capability.

2.2.2 Coordinate system

The commonly chosen coordinate system for a circular particle collider is a right-handed system with the z-axis parallel to the beam direction and perpendicular to the (x, y) plane. The x-axis is chosen to point towards the centre of the collider.

For track measurements, the azimuthal angle ϕ measured in the (x, y) plane and polar angle θ measured from the positive part of z-axis. Instead of the θ angle, a quantity called pseudorapidity η is used, defined

$$\eta = -\log\left(\tan\frac{\theta}{2}\right). \tag{2.9}$$

To give an illustration: a particle produced perpendicularly to the beam direction has zero pseudorapidity. The particle production is a constant function of η. Moreover, the difference in η is, unlike the difference in θ, Lorentz-invariant.

Distances are measured in the (η, ϕ) plane as the Euclidean norm $\Delta R^2 = \Delta\eta^2 + \Delta\phi^2$.

2.2.3 Transverse momentum

The transverse momentum p_{T} lies in the (x, y) and it is defined as

$$p_{\mathrm{T}} = \sqrt{p_x^2 + p_y^2}. \tag{2.10}$$

It is also Lorentz-invariant along the z-axis.

It is always associated with physics at the collision, as the beams are collimated in a way to eliminate p_{T} before the collision. If it is zero before the collision, then due to conservation of momentum, after collision it must stay zero and so most physics can be derived from the p_{T}.

The missing transverse energy $\not{E}_{\mathrm{T}}$ is attributed to presence of neutrinos in the interaction. It is defined as the sum of the transverse momenta of all reconstructed tracks:

$$\not{E}_{\mathrm{T}} = -\sum_i p_{\mathrm{T}}(i). \tag{2.11}$$

2.2.4 Luminosity

Luminosity is another important property of a collider. It gives a number of particles passing through a unit area of the interaction region per unit

time. In other words, it characterizes the number of produced collisions. The crossing rate f of two bunches containing n_1 and n_2 is the frequency of how often these bunches pass one another. The luminosity $\mathcal{L}$ is given by

$$\mathcal{L} = f \frac{n_1 n_2}{4\pi\sigma_x\sigma_y}, \tag{2.12}$$

where σ_x, σ_y are Gaussian transverse beam profiles in the x and y direction.

The number of events N_{exp} produced with the desired cross section σ_{exp} is proportional to the integrated luminosity, where time integration is assumed:

$$N_{\text{exp}} = \sigma_{\text{exp}} \int \mathcal{L}(t)\,\mathrm{d}t. \tag{2.13}$$

2.3 Large Hadron Collider

Presently, the largest and most powerful particle accelerator in the world is the Large Hadron Collider (LHC), part of the accelerator complex at European Organization for Nuclear Research (CERN[1]). Situated beneath the Franco-Swiss border with the headquarters located near Geneva, it was installed in a circular tunnel of 26.6 km in circumference, 3.8 m in width and 175 m in maximum depth.

The collider tube consists of two separate parallel beam pipes with four intersection points, where the four main experiments are located. In both beam pipes, two beams travel in opposite directions. Beams are made up of either protons or lead nuclei. Each beam consists of bunches that are of 10^{-2} m in length and 10^{-5} m in diameter, separated in time by 25 ns (which translates to the peak crossing rate of 40 MHz).

ATLAS, „A Toroidal LHC ApparatuS“, serves as a general purpose experiment exploring physics at energies in the TeV range. Main areas of research are Higgs boson and t quark properties, B-physics, searching for new particles and new physics phenomena.

CMS, „Compact Muon Solenoid“, is the other general purpose detector. Though it differs from ATLAS in technical design, it shares similar physics goals, so that new findings can be either validated or disproved.

ALICE, „A Large Ion Collider Experiment“, focuses on heavy ion (lead nuclei) collisions. Such collisions are believed to be capable of QGP production.

LHCb, „Large Hadron Collider beauty“, is optimized for B-physics experiments, specifically rare B_s and B_d decays. As B mesons travel mostly forward along the beamline, the layout of the experiment is designed asymmetrically with respect to the interaction point, as a single-arm detector in the forward region.

[1] The acronym comes from the original title *Conseil Européen en pour la Recherche Nucleaire.*

2.3.1 Beam energy

At the initial period of operation (2010), beam energy reached 3.5 TeV, and in 2012, when the data for this thesis were collected, collisions were occurring at 4 TeV per beam. In 2015, after a two-year shut down, beam energy reached 6.5 TeV. The LHC aims for maximum energy of 7 TeV per beam, leading to the centre-of-mass energy of $\sqrt{s} = 14$ TeV.

To reach these high energies, a proton beam is accelerated in several pre-accelerators. At first, protons are stripped of electrons. They are then directed to the Linear Accelerator (Linac2), where they gain energy of 50 MeV. Afterwards, the beam heads to the Proton Synchrontron Booster (PSB) capable of accelerating the protons to 1.4 GeV, followed by the Proton Synchrotron (PS) and the Super Proton Synchrotron (SPS), which are capable of accelerating them further – up to 25 GeV and 450 GeV, respectively. At this stage, they have enough energy to be injected to the LHC and accelerated there.

The lead ions are obtained from vaporized lead. They start their way in the Linac3 accelerator. Afterwards, they are collected by Low Energy Ion Ring (LEIR) and injected to the Proton Synchrotron, where they follow the same route as the protons onwards.

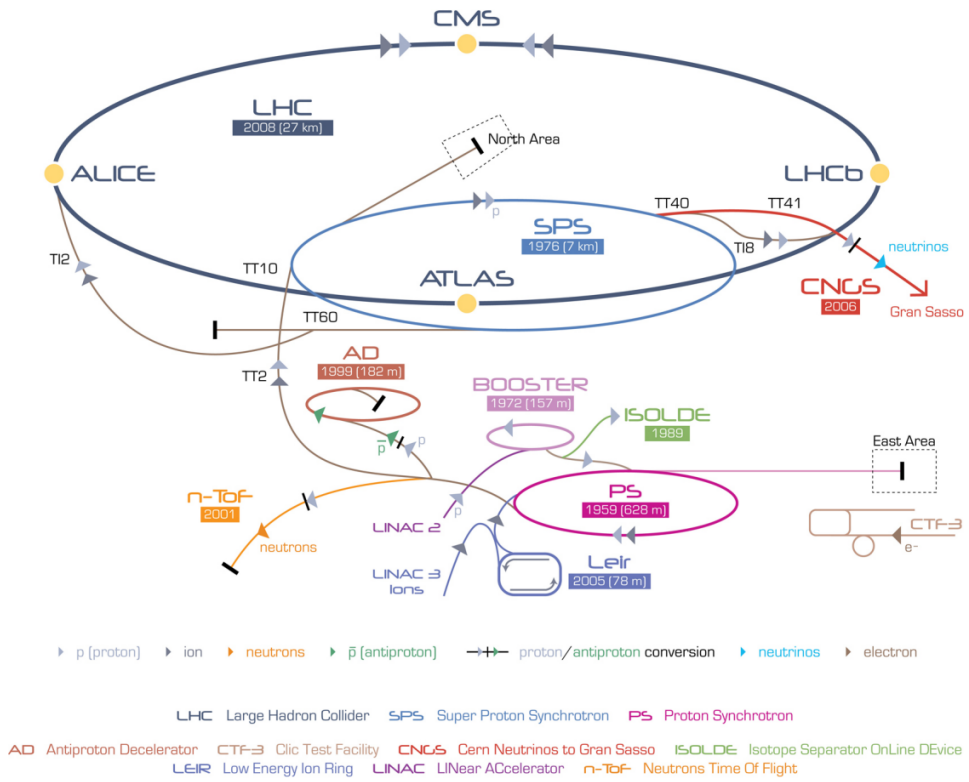

Fig. 2.1: The LHC accelerator complex with description. [4]

During the planned two-year shut down, the pre-accelerator system has undergone several upgrades to allow for the increase of the beam energy. This required the enhancement of the PS and SPS as well as the cabling and the

cooling system. Meanwhile, upgrades of the detectors took place during that period.

2.4 ATLAS detectors

The ATLAS detector is a cylindrical detector, symmetric with respect to the collision point. It can be divided into the barrel and end-cap regions. End-caps are located at the ends of the cylinder, in form of disks perpendicular to the beam axis, and the barrel region is situated in between, consisting of several concentric cylindrical layers. Outside the detector, a massive magnet system is placed, and the detector itself consists of various subsystems that cover different ranges of η, the maximum being $|\eta| < 4.9$.

In the innermost layer, the Inner Detector is located, covering $|\eta| < 2.5$. Its main purpose is tracking and particle type detection. In the layer above, electromagnetic and hadronic calorimeters are situated, measuring energy of particles that interact electromagnetically or strongly. Calorimeters combined cover the maximum η range. The muon spectrometer is the outermost detector, covering $|\eta| < 2.7$. It serves as a muon track detector.

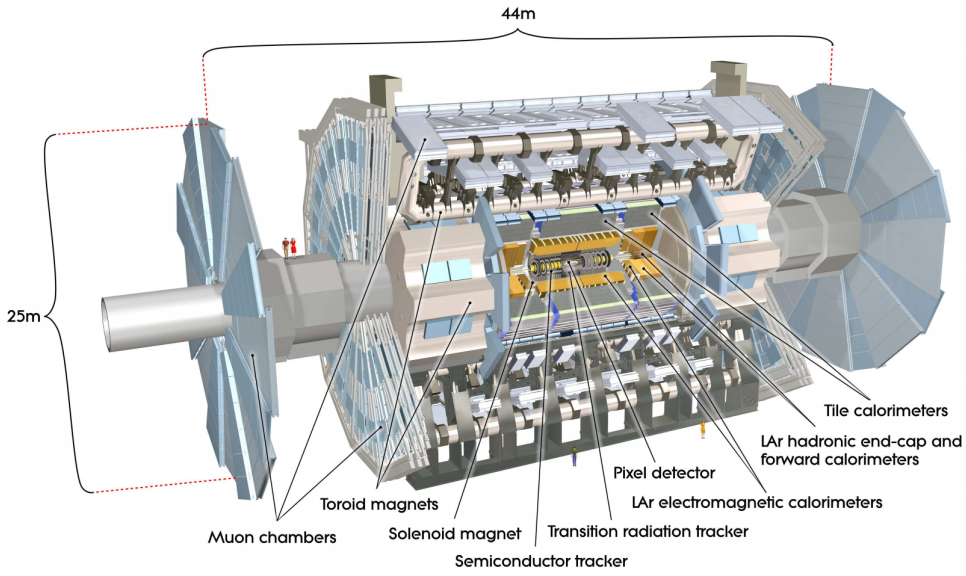

Fig. 2.2: ATLAS detector with description, cut-away view. [5]

2.4.1 Magnet system

ATLAS has an extraordinary superconducting magnet system capable of generating magnetic field of 2 T. The magnets have to be cooled to very low temperatures. Field of this strength is capable of curving even the lightest of charged particles, via the effect of the Lorentz force. From the radius of the curvature, the particle momentum can be calculated. There are three main

components of the magnet system. The central solenoid encases the Inner Detector. The barrel and end-cap toroids are placed around the calorimeters.

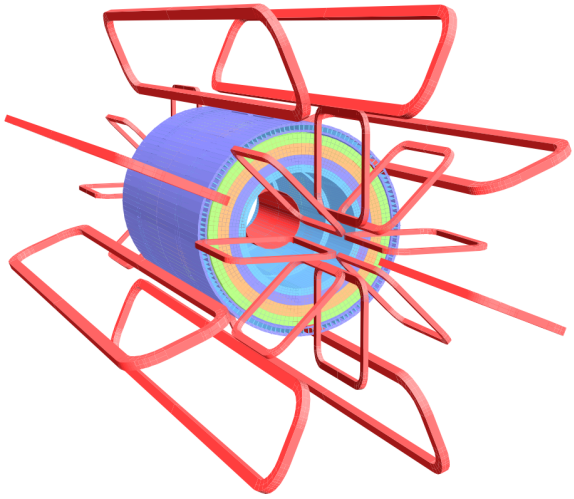

Fig. 2.3: ATLAS magnet system, schematic view. Coils (red) and calorimeters (other colours) are visible. [5]

2.4.2 Inner detector

The Inner Detector (ID) plays pivotal role in track reconstruction (tracking) – it registers the exact position of hits of the incoming particle in subsequent layers. This results in visualization of the tracks of charged particles and their partial identification. In order to maximise the η range, the ID has a barrel and end-cap section, and to maximise efficiency, it consists of three different subsystems.

Pixel detector

The Pixel detector is situated as close as 3.3 cm from the interaction point. This allows for precise measurements, such as detection of short-lived particles as B mesons. This way, impact parameters can be extracted.

The barrel section consists of four layers, the first one called the insertable b-layer (IBL) is the closest to the beampipe. It was added during the recent LHC shutdown, inserted between the beampipe and the now second innermost b-layer.

On these layers, staves that contain cells of silicon pixel modules are placed in an overlapping fashion. Depending on particle curvature, this will ideally yield four or more points of the particle trajectory. End-caps consist of three disks each with the same pixel detectors.

A charged particle traversing a cell liberates a hole/electron in the material, which propagates a signal leading directly to the front-end electronics. To ensure optimal performance, system is cooled to temperatures slightly below 0 °C.

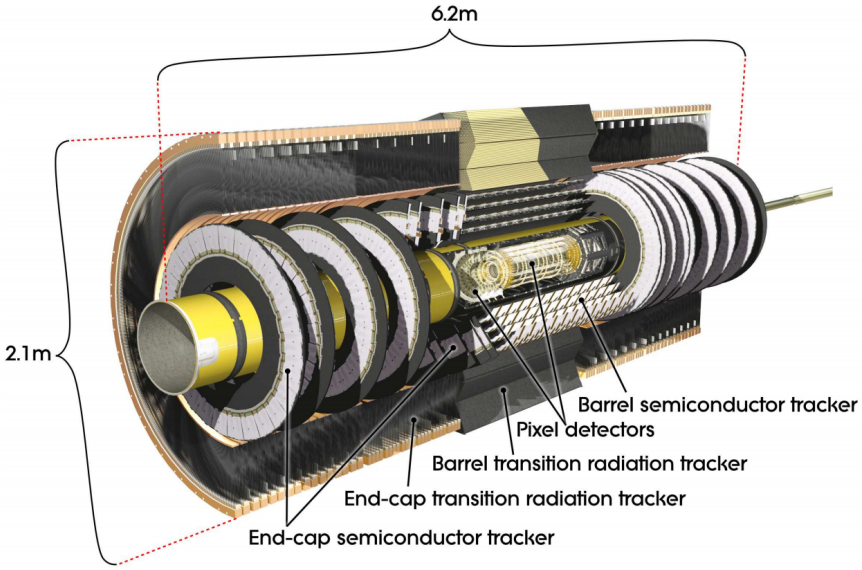

Fig. 2.4: ATLAS Inner Detector with description, cut-away view. [5]

Semiconductor Tracker

The Semiconductor Tracker (SCT) is similar to the Pixel detector in design. In the barrel region, there are four layers of double silicon microstrip detectors of rectangular shape, mounted in parallel to the beam axis. Each end-cap contains nine layers of strips of wedge shape.

In an ideal case, the detector registers at least 4 hits per track, providing precise measurement in the (R, ϕ) plane, the precision being smaller on the z-axis.

Transition Radiation Tracker

The Transition Radiation Tracker (TRT) serves a different purpose from the remaining two inner subdetectors. It detects the particle type by measuring the ionizing energy loss, or more specifically, the transition radiation.

Barrel region accommodates 73 layers of drift straw tubes, and the end-caps contain 160 of these, reaching a total number of almost 400 000 straws. The straws are filled with mostly xenon gas (at high voltage) and equipped with a gold-plated anode. A charged particle passing through a straw ionizes the gas inside, creating a drift of ions along the potential, heading towards the anode and creating a signal.

Due to high amount of detectors, particle traverses the TRT 36 times in average. The downside is that only the (R, ϕ) coordinates are granted. TRT is efficient in electron identification, as light charged particles are more prone to transition radiation and bremsstrahlung.

2.4.3 Calorimeters

Calorimetry is provided by detectors that measure the energy of incoming particles by absorption. The detector is thus an active medium for some particles, whereas it permits muons (and neutrinos, naturally) to pass through. The deposited energy in the material is used for secondary particle production, those then produce tertiary particles and this goes on. This is called a particle shower.

Measured energy yields information concerning the kinematic properties of the particle. Aside from that, calorimeters can tell hadrons and electrically charged particles apart, and identify neutrinos by the means of missing transverse energy $\not{E}_{\mathrm{T}}$. As hadrons are less easily absorbed, Hadronic Calorimeters are placed outside the Electromagnetic Calorimeter.

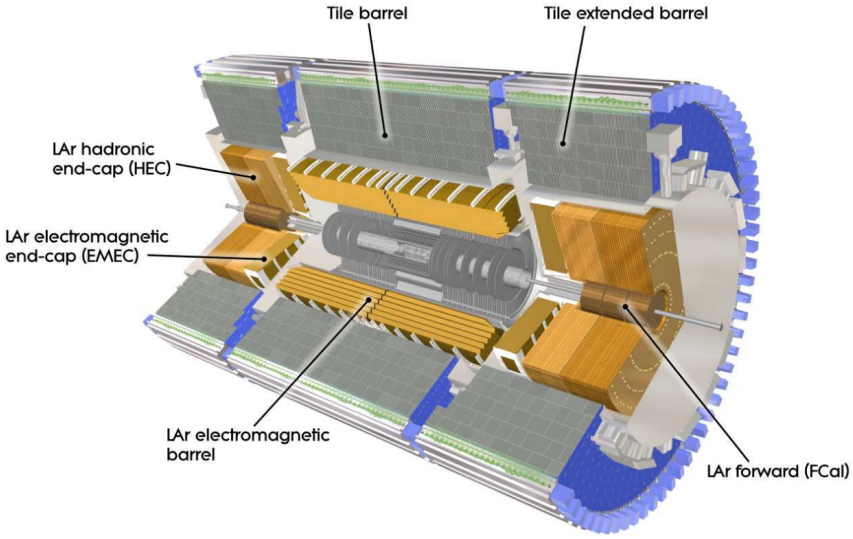

Fig. 2.5: ATLAS calorimeters with description, cut-away view. [5]

Electromagnetic Calorimeter

The Electromagnetic Calorimeter is designed to contain showers of charged particles. These showers usually emerge as a cascade of electron bremsstrahlung and $e^{-}e^{+}$ production.

The calorimeter is made from lead and liquid argon. Lead plates serve as the absorber medium and the liquid argon as the active material, altogether called LAr. The electrons produced in the shower are carried in the LAr and detected on readout electrodes located in between the absorbers. LAr must be cooled at $-183\,^{\circ}\mathrm{C}$.

Altogether, the barrel and end-caps regions cover $|\eta| < 3.2$, and despite higher granularity in the lateral regions, they remain precise enough for measurement.

Hadronic Calorimeters

Hadronic Calorimeters comprise three subsystems. In the barrel region, the scintillator tile calorimeter is located, which is extended in the forward region. On the end-caps, LAr calorimeters are used, design of which is similar to that of Electromagnetic Calorimeter. An additional LAr calorimeter is installed in the forward region, providing maximum η range $|\eta| < 4.9$.

Hadronic Calorimeters are designed to contain hadron showers. The barrel detector uses steel as the absorber medium and scintillating tiles as the detection medium. The readout of the tiles is performed using so-called wavelength shifting fibres, which send the signal to the photomultiplier tubes.

The end-cap detector uses liquid argon with copper in place of lead. It is also capable of muon detection. The forward LAr calorimeter utilizes copper (for electromagnetic detection) and tungsten (for hadron detection) as the absorber.

2.4.4 Muon spectrometer

Due to low muonic radiation losses (1 MeV/1 mm) and relatively long lifetime, the muon detectors are placed in the outermost detector layer. Situated in barrel and end-cap regions, their purpose is to measure both trajectory and momentum of muons. Their secondary purpose is to trigger events.

Monitored Drift Tube chambers

The Monitored Drift Tube chambers (MDT) provides the track measurement in the $|\eta| < 2.7$ range with a precision of tens of μm. Drift tubes, arranged in three layers, are made of aluminium and filled with mostly argon. The principle of detection is the same as in TRT. The resulting trajectory determines the charge and momentum of the muon, as oppositely charged particles will curve in different direction. MDT exhibits a rather high reliability – the failure of a single tube out of 1150 tubes will not render the detector unusable.

Cathode Strip Chambers

The Cathode Strip Chambers (CSC) are advantageous for high particle fluxes, which are expected to occur at $2.0 < |\eta| < 2.7$. They are multi-wire proportional chambers with perpendicularly placed cathode strips. A muon traversing the detector will induce a charge in the surrounding cathodes. The detector has a slightly higher granularity in comparison to the MDT.

Resistive Plate Chambers

The Resistive Plate Chambers (RPC) complement the rest of the system. They are used mainly for triggering purposes. Their design is similar to MDT, three layers being capable of detecting muons with p_{T} in given intervals $(6, 9)$ GeV and $(9, 35)$ GeV. The detection is very fast and efficient. The azimuthal angle ϕ is also measured by RPC.

Thin Gap Chambers

The Thin Gap Chambers (TGC) are located at the end-caps, as a multi-wire proportional chambers. The distance between cathodes is smaller than the wire-to-wire distance. They share the same purpose as RPC (triggering and ϕ measurement), but offer even better time resolution.

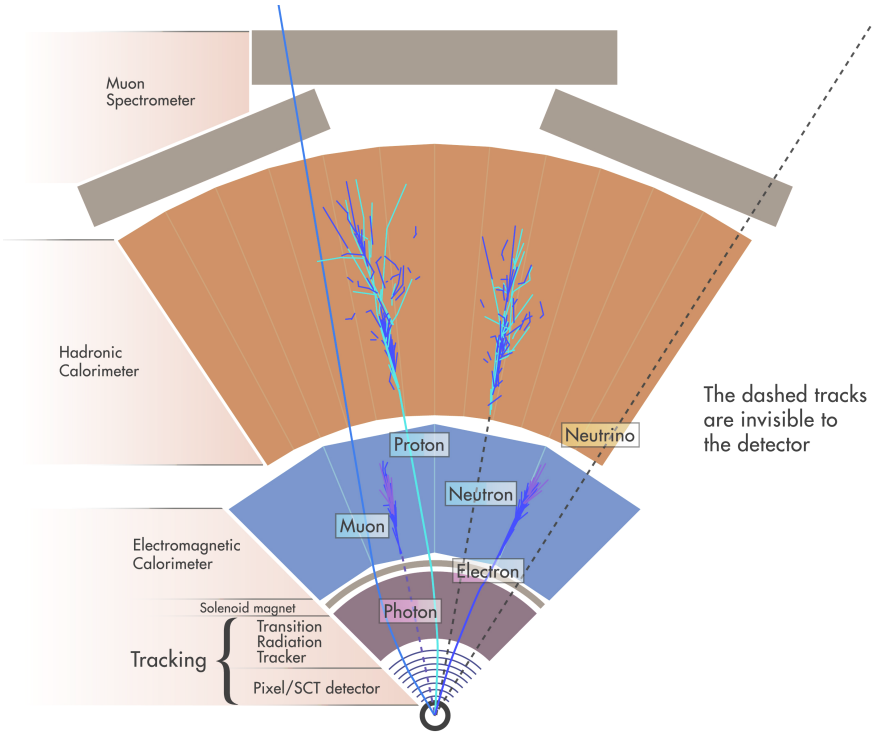

Fig. 2.6: ATLAS detector layers and particle propagation. [6]

Chapter 3

B-physics

3.1 History

In the early 1970s, Japanese theoretical physicists M. Kobayashi and T. Maskawa suggested the existence of a third quark generation [13].[1] It was indeed observed few years later at Fermilab, starting with the b quark in the bottomonium bound state. In 1980, first B mesons emerged and their unusual properties sparked the interest in the HEP community, leading to the now well-established field of B-physics.

The study of the B mesons and their decays proved fruitful as it improved the understanding of hadronic processes. It continues exploring and testing the Standard Model predictions and through this it opens the way for potentially new physics phenomena, should the predictions prove wrong.

For this reasons, two colliders with a single purpose of producing B mesons were built, called B-factories: the Belle experiment at the KEKB collider in Japan, and the BaBar experiment at SLAC laboratory in the USA. Both B-factories ceased operation in 2010 and 2008, respectively. A successor to the Belle experiment, Belle II, is currently under construction.

3.2 Related concepts

3.2.1 Flavour mixing

Fermions appearing in the Standard Model are characterized either by their mass eigenstates or interaction eigenstates. The mass eigenstate is the quantum state of a particle which propagates in free space, whilst the interaction eigenstate is a different state that participates in electroweak interactions. It is conventional to define the neutrino flavour by the interaction eigenstate and the quark flavour by the mass eigenstate. To switch between these states, we use the Cabibbo-Kobayashi-Maskawa (CKM) matrix (in the case of quarks) or the Pontecorvo–Maki–Nakagawa–Sakata (PMNS) matrix (in the case of neutrinos).

[1] This famous article stays among the top most highly cited articles of all time. [14]

The dimensions of these matrices are given by the number of generations in the Standard Model. Before the b and t quarks were known, the matrix existed in a two-dimensional form. It was named after N. Cabbibo, who was the first one to notice the discrepancy between the mass and interaction eigenstates of the d quark, postulating that the weak interaction couples differently to distinct quark generations.

3.2.2 CKM matrix

Let (d', s', b') denote the interaction eigenstates and (d, s, b) the mass eigenstates of the d, s, and b quarks. The CKM matrix by convention acts on quarks with charge $-\frac{1}{3}e$. It is a unitary matrix with complex elements in the form

$$\begin{pmatrix} d' \\ s' \\ b' \end{pmatrix} = \begin{pmatrix} V_{ud} & V_{us} & V_{ub} \\ V_{cd} & V_{cs} & V_{cb} \\ V_{td} & V_{ts} & V_{tb} \end{pmatrix} \begin{pmatrix} d \\ s \\ b \end{pmatrix}, \tag{3.1}$$

where each matrix element V_{ij} corresponds to the decay amplitude of j quark weakly decaying into i quark. Their values are not predicted by the Standard Model and so they have to be determined experimentally. Usually, the CKM matrix is parametrised by three angles and a non-trivial complex phase.

When evaluating the magnitude of the matrix elements, the matrix turns out to be nearly diagonal, i.e. $|V_{ud}| \approx |V_{cs}| \approx |V_{tb}| \approx 1$. Because of this, generation-conserving weak decays are preferred. Any other decays are suppressed, but their probability is non-zero. The matrix also allows the weak interaction to violate the flavour conservation.

3.2.3 *CP* violation

It was believed that the laws of physics were C and P symmetric – invariant to single $\hat{\mathrm{C}}$ or $\hat{\mathrm{P}}$ transformations. It held true until the weak interaction was found to violate the P symmetry – weak interaction acts on left-handed particles (or right-handed antiparticles) only.

An important discovery was made on the neutral kaon decays. As weak interactions does not conserve strangeness, neutral kaon $K^0 = d\bar{s}$ can transform into its antiparticle $\bar{K}^0 = s\bar{d}$ and vice versa. This makes the measurement of their lifetime troublesome as they cannot be considered independent objects.

Let us now assume that the symmetry under combined CP symmetry holds. Acting with $\hat{\mathrm{C}}$ and $\hat{\mathrm{P}}$ operators on the kaon wavefunction $\left|K^0\right\rangle$, we obtain

$$\hat{\mathrm{C}}\left|K^0\right\rangle = +\left|\bar{K}^0\right\rangle, \qquad \hat{\mathrm{P}}\left|K^0\right\rangle = -\left|K^0\right\rangle, \tag{3.2}$$

as K^0 has odd parity. Using the combined operators $\hat{\mathrm{C}}\hat{\mathrm{P}}$, we obtain the same wavefunction with an opposite sign:

$$\hat{\mathrm{C}}\hat{\mathrm{P}}\left|K^0\right\rangle = -\left|\bar{K}^0\right\rangle. \tag{3.3}$$

Let us propose the following superpositions of K^0 and $\bar{K}^0$ states:

$$\left|K_1^0\right\rangle = \frac{1}{\sqrt{2}}\left(\left|K^0\right\rangle - \left|\bar{K}^0\right\rangle\right), \qquad \left|K_2^0\right\rangle = \frac{1}{\sqrt{2}}\left(\left|K^0\right\rangle + \left|\bar{K}^0\right\rangle\right). \tag{3.4}$$

The $\hat{\mathrm{C}}\hat{\mathrm{P}}$ operator will map these new wavefunctions onto themselves.

$$\hat{\mathrm{C}}\hat{\mathrm{P}}\left|K_1^0\right\rangle = +\left|K_1^0\right\rangle, \qquad \hat{\mathrm{C}}\hat{\mathrm{P}}\left|K_2^0\right\rangle = -\left|K_2^0\right\rangle, \tag{3.5}$$

in other words, the $|K_1^0\rangle$ is an odd CP eigenstate and $|K_2^0\rangle$ an even CP eigenstate.

Provided the CP symmetry holds, these particles decay in a different way: $K_1^0 \to \pi\pi$ and $K_2^0 \to \pi\pi\pi$, because the three pion system is an odd CP eigenstate and two pion system is an even CP eigenstate:

$$\hat{\mathrm{C}}\hat{\mathrm{P}}\left|\pi\pi\right\rangle = +\left|\pi\pi\right\rangle, \qquad \hat{\mathrm{C}}\hat{\mathrm{P}}\left|\pi\pi\pi\right\rangle = -\left|\pi\pi\pi\right\rangle. \tag{3.6}$$

Pion signs are omitted because any combination which results in a zero electric charge is permitted. As the three pion decay is more complicated, K_2^0 has a longer lifetime compared to the K_1^0. At a long distance from the production point, the K_1^0 decaying into two pions should no longer be observed. Yet, in 1964, Cronin and Fitch observed a small number of $K_2^0 \to \pi^+\pi^-$ decays, which is a contradiction of our initial assumption. Weak interaction therefore violates the CP symmetry. This effect is known as the CP violation.

It turns out that the K_1^0 and K_2^0 are not quite the CP eigenstates. Instead, particles K_S^0 and K_L^0 defined as

$$\left|K_S^0\right\rangle = \frac{1}{\sqrt{1+|\varepsilon|^2}}\left(\left|K_1^0\right\rangle + \varepsilon\left|K_1^0\right\rangle\right) \tag{3.7}$$

$$\left|K_L^0\right\rangle = \frac{1}{\sqrt{1+|\varepsilon|^2}}\left(\varepsilon\left|K_1^0\right\rangle + \left|K_2^0\right\rangle\right) \tag{3.8}$$

are the true CP eigenstates, with $|\varepsilon| \approx 10^{-3}$. Their lifetime is denoted by the subscript – short (K_S^0) or long (K_L^0).

The second source of CP violation comes from the difference in the K^0 and $\bar{K}^0$ decay amplitudes. Together, they contribute to the CP violation that is observed in the neutral kaon decay. Similar incidence has been found in beauty and charm meson decays.

CP violation is thought to be the culprit of the baryon asymmetry, as it is a plausible explanation on what caused the particle-antiparticle symmetry to slightly break. This slight imbalance would possibly cause the slow diminishing of antimatter, creating the matter-abundant world as we know it today.

3.3 Neutral B mesons

The B mesons are unique in a number of reasons. They are relatively long lived and they have high invariant masses. Moreover, due to the b quark being more massive than anything it decays into, the corresponding b–jets have high multiplicities and contain particles with high p_{T}.

Neutral mesons containing beauty particles are the $B_s = s\bar{b}$ and $B_d = d\bar{b}$, with the B_s being slightly heavier. They are spontaneously oscillating into one another as well. This can be visualised using the following box diagram.

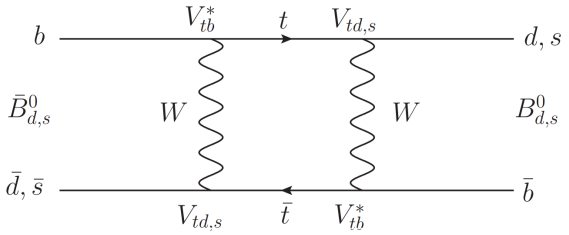

Fig. 3.1: Box diagram depicting neutral B meson mixing. A CKM matrix element is assigned to each vertex. [7]

The neutral B mesons can decay using the $B_d \to J/\psi K^{*0}$ and $B_s \to J/\psi\phi$ channels. This work is focused on the $B_s \to J/\psi(\mu^+\mu^-)\phi(K^+K^-)$ decay channel, which is commonly studied because of its potential for the extraction of the parameters that are relevant for the CP violation study. The branching ratio of this decay channel is $(1.07 \pm 0.09) \cdot 10^{-3}$.

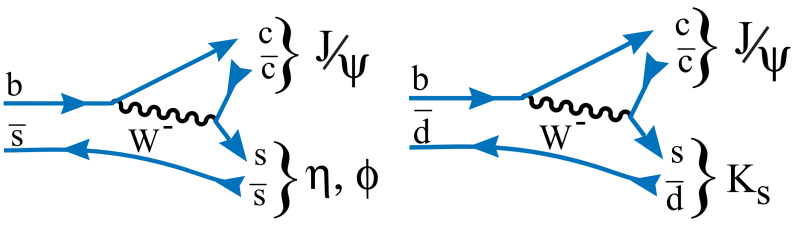

(a) : B_s decay **(b) :** B_d decay

Fig. 3.2: Examples of decay channels of neutral B mesons. [8]

The B_s and $\bar{B}_s$ mesons manifest themselves as two mass eigenstates B_1 and B_2 in analogy with neutral kaons. The CP eigenstates (which are not the B_1 and B_2) are the heavy B_H and light B_L beauty mesons.

3.4 *B*-physics at ATLAS

Although there is one experiment on the LHC tailored for B-physics – LHCb experiment, ATLAS has its own B-physics programme is able to compete with LHCb. There are no first-hand systems at ATLAS that would separate kaons from muons and thus the LHCb provides a clearer signal (thinner peaks). Moreover, most B meson related interactions happen in the forward region, which is also in favour of LHCb. On the other side, ATLAS runs on the maximum luminosity (LHCb is deliberately limited by lower luminosity to keep the background (pile-up) low).

There are two aspects of B-physics at ATLAS: heavy flavour particle production (and their production cross section measurements), and exclusive B meson decays (mainly via di-muon channels[2]).

[2]Such channels are used mainly because of the extensive muon detector systems at ATLAS.

Chapter 4

Data analysis

4.1 Fit method

When dealing with large number of data points, it is easier to work with a binned histogram, which groups data into bins according to their multiplicity. This is not recommended for small datasets as a lot of information will be lost this way. To find a trend in the data, one can perform the 'unbinned maximum likelihood fit', which treats each data point as a bin on its own.

Unbinned maximum likelihood fits are used even for large datasets. This is motivated by having each data point characterized by more than two observables. In this case, the bins are populated with a small number of data points, and so there is a large number of bins. The computational cost is then on par or slightly higher compared to a binned fit.

4.1.1 Probability density function

In the experiment, observables $\boldsymbol{x}$ are measured. Physical parameters of interest and other parameters are determined by $\boldsymbol{p}_0$. The function that describes the frequency of occurrence of $\boldsymbol{x}$ is the continuous probability density function, $F(\boldsymbol{x};\boldsymbol{p}_0)$ (PDF for short). To estimate $\boldsymbol{p}_0$ with our fit, we define a general vector $\boldsymbol{p}$ and vary it to match the actual shape.

The fundamental properties of a probability density function are positive definiteness and the normalization over the whole range of observables, which is assumed for all parameters $\boldsymbol{p}$,

$$\int_{\boldsymbol{x}_{\min}}^{\boldsymbol{x}_{\max}} F(\boldsymbol{x};\boldsymbol{p})\,\mathrm{d}\boldsymbol{x} = 1, \quad \forall \boldsymbol{p}. \tag{4.1}$$

The expression $F(\boldsymbol{x};\boldsymbol{p}_0)\,\mathrm{d}\boldsymbol{x}$ is the probability that for a given event with parameters $\boldsymbol{p}_0$, the observables $\boldsymbol{x}$ will fall in the range $\mathrm{d}\boldsymbol{x}$. Compare this with the expression $F(\boldsymbol{x};\boldsymbol{p}_0)\,\Delta\boldsymbol{x}$, which gives the mean probability over the bin $\Delta\boldsymbol{x}$.

Normalizing takes a lot of effort for a PDF in dimensions larger than one. It is usually performed by assuming $\int F(\boldsymbol{x};\boldsymbol{p})\,\mathrm{d}\boldsymbol{x} = N$ and absorbing the normalization constant N into the vector of parameters, $\boldsymbol{P} = (N, \boldsymbol{p})$.

4.1.2 Likelihood function

The probability density function $F(\boldsymbol{x}_0; \boldsymbol{p})$ evaluated at a fixed data point $\boldsymbol{x}_0$ and taken as a function of parameters $\boldsymbol{p}$ defines the likelihood function, or simply likelihood

$$L(\boldsymbol{p}) = L(\boldsymbol{p}; \boldsymbol{x}_0) = F(\boldsymbol{x}_0; \boldsymbol{p}). \tag{4.2}$$

Comparing the two terms, a probability density function is an estimation of the data based on the given parameters, whereas in the likelihood, the parameters are unknown and their values are determined from the measured data. Our goal is to maximize likelihood, and thus maximize the concordance of the physics model and measured data.

For an experiment consisting of multiple events indexed by i, likelihood is defined simply as the product of single-event likelihood functions, probabilities $F(\boldsymbol{x_i}; \boldsymbol{p})$.

$$L(\boldsymbol{p}) = \prod_i F(\boldsymbol{x_i}; \boldsymbol{p}). \tag{4.3}$$

This defines the *unbinned* likelihood function for the probabilities $F(\boldsymbol{x_i}; \boldsymbol{p})$ are taken for each data point without binning.

It is easier to work with a log-likelihood as it simplifies the product into a sum,

$$\log\left(L(\boldsymbol{p})\right) = \sum_i \log(F(\boldsymbol{x_i}; \boldsymbol{p})). \tag{4.4}$$

Maximizing likelihood is then equal to finding $\boldsymbol{p}$ that minimizes the negative log-likelihood,

$$\frac{\partial \log L(\boldsymbol{p})}{\partial \boldsymbol{p}} = 0. \tag{4.5}$$

Such a set of parameters $\boldsymbol{p}$ is called a maximum likelihood estimator, and it gives the shape of the PDF that approximates data the best. Using this technique, we can find the desired PDF without knowing the parameters beforehand.

The following notation is often used when working with PDFs. The $\cup$ symbol denotes the logical `OR` operator, comma will be used as the logical `AND` operator. Using this notation, $P(A, B)$ indicates the probability of events A and B occurring at once, and $P(A \cup B)$ indicates the probability that either A or B will occur. The following relation defines the conditional probability:

$$P(A|B) = \frac{P(A, B)}{P(B)} \tag{4.6}$$

and it should be read as the probability of A given B. This notation is often abused to enable expressions such as $P(x|S)$ and $P(x|B)$, which should be taken as the probability of variable x being the signal S or the background B.

The probability density function $P(\boldsymbol{x_i}, S \cup B)$ used to account for a signal and a background occurrence in the event i assumes the form

$$\begin{aligned} P(\boldsymbol{x_i}, S \cup B) &= P(\boldsymbol{x_i}, S) + P(\boldsymbol{x_i}, B) \\ &= P(S) \cdot P(\boldsymbol{x_i}|S) + P(B) \cdot P(\boldsymbol{x_i}, |B) \\ &= f \cdot P(\boldsymbol{x_i}|S) + (1 - f) \cdot P(\boldsymbol{x_i}|B). \end{aligned} \tag{4.7}$$

The first equality represents the mutual exclusivity of events S and B – the signal events cannot concurrently depict the background. The second equality was treated with Eq. (4.6); and the third is based on the following assumption: if both $P(\boldsymbol{x_i}|S)$ and $P(\boldsymbol{x_i}|B)$ are normalized, then $P(S) + P(B) = 1$ in order for $P(\boldsymbol{x_i}, S \cup B)$ to be normalized likewise. The $f = P(S)$ is then the fraction of events in the data that are signal-like.

The likelihood is

$$L = \prod_i \{f \cdot P(\boldsymbol{x_i}|S) + (1 - f) \cdot P(\boldsymbol{x_i}|B)\}, \tag{4.8}$$

where $P(\boldsymbol{x_i}|S) = F_{\text{sig}}(\boldsymbol{x_i}; \boldsymbol{p})$ is the model of signal distribution, parametrised by $\boldsymbol{p}$; and $P(\boldsymbol{x_i}|B) = F_{\text{bkg}}(\boldsymbol{x_i}; \boldsymbol{q})$ the model of background distribution, parametrised by $\boldsymbol{q}$.

We will now restrict ourselves to one-dimensional case. The model distribution can be a Gaussian normal distribution (4.9), where $\boldsymbol{x_i} = x_i$ and $\boldsymbol{p} = (\mu, \sigma)$ (parameter dependence is given by the mean μ and width σ).

$$G(x_i; \mu, \sigma) = \frac{1}{\sigma\sqrt{2\pi}} \exp\left\{-\frac{(x_i - \mu)^2}{2\sigma^2}\right\}. \tag{4.9}$$

4.1.3 Punzi terms

There are certain pitfalls when dealing with likelihoods with conditional probabilities. Suppose that we have a likelihood function (4.8) with the signal and background models as Gaussians (4.9) with fixed width σ and means μ_1, μ_2 during the course of the experiment:

$$L = \prod_i \{f \cdot G(x_i; \mu_1, \sigma) + (1 - f) \cdot G(x_i; \mu_2, \sigma)\}. \tag{4.10}$$

The width is usually dependent on the detector resolution, which is not constant in practice. One could assume that we could vary the width the event-by-event, leading to the likelihood

$$L = \prod_i \{f \cdot G(x_i; \mu_1, \sigma_i) + (1 - f) \cdot G(x_i; \mu_2, \sigma_i)\}. \tag{4.11}$$

Notice the σ_i instead of fixed σ. More information was used and so a better fit result would be naturally expected. Surprisingly, this is not the correct likelihood function. The reason is because the expression

$$P(x_i) = f \cdot G(x_i; \mu_1, \sigma_i) + (1 - f) \cdot G(x_i; \mu_2, \sigma_i) \tag{4.12}$$

is, in fact, not the probability to find x_i, but the probability to find x_i given σ_i – in a nutshell, that is conditional probability $P(x_i|\sigma_i)$. Recall that $P(x_i) \neq P(x_i|\sigma_i)$. With this in mind, σ_i has to be added as a measurement.

Let $G(x_i;\sigma_i,\mu_1) = P(x_i,\sigma_i|S)$ denote the signal model and $G(x_i;\sigma_i,\mu_2) = P(x_i,\sigma_i|B)$ the background model. Note that the σ_i have been shifted from a parameter to an argument. The right treatment of the probability is as follows,

$$\begin{aligned} P(x_i,\sigma_i,S\cup B) &= P(x_i,\sigma_i,S) + P(x_i,\sigma_i,B) \\ &= P(S)\cdot P(x_i,\sigma_i|S) + P(B)\cdot P(x_i,\sigma_i|B) \\ &= f\cdot P(x_i,\sigma_i|S) + (1-f)\cdot P(x_i,\sigma_i|B) \\ &= f\cdot P(x_i|\sigma_i,S)\cdot P(\sigma_i|S) + (1-f)\cdot P(x_i|\sigma_i,B)\cdot P(\sigma_i|B). \end{aligned}$$

In the last step, Eq. (4.6) was used to „shift“ the σ_i back to the parameters. Compared to Eq. (4.8), the correct form of likelihood is

$$L = \prod_i \{f\cdot P(x_i|\sigma_i,S)\cdot \underline{P(\sigma_i|S)} + (1-f)\cdot P(x_i|\sigma_i,B)\cdot \underline{P(\sigma_i|B)}\}. \quad (4.13)$$

The underlined terms are called the Punzi terms. They are hidden in the definition (4.8), because in case of $P(\sigma|S) = P(\sigma|B)$, these terms can be factored out as a constant factor and thus be ignored in the maximization. Omitting the Punzi terms generally leads to a bias. More information about Punzi terms including simple example of such a bias can be found in [15].

4.2 Software

4.2.1 ROOT framework

ROOT is a stand-alone object-oriented framework developed at CERN as a toolkit for particle physics data analysis. It can perform various tasks such as data visualisation, histogram plotting and fitting, regression analysis, function minimization and various other calculations. ROOT is very efficient in handling large amounts of data and it partially supports parallel computing. It utilizes C++ as the commanding and scripting language. Commands can be either typed directly into the CINT command line in the interpreter mode, or they can be written in macros that can be executed or compile. It is distributed as a free software, under general public license.

4.2.2 RooFit

RooFit is an add-on library augmenting and complementing the ROOT environment as one can use any of the ROOT objects while using RooFit. It is designed for extensive data analysis, provides classes designed to make fitting easier. It can also easily generate ‘toy Monte Carlo’ data samples. Even though it is mainly B-physics related, as it was originally developed for

the BaBar experiment, its general nature makes it useful in other branches of physics, where large amounts of data are processed.

RooFit naturally operates with probability density functions and takes care of their normalization, and performs unbinned maximum likelihood fits, which is of interest in this thesis. For this purpose, it supports a large number of probability density functions, that are not naturally included in ROOT, and users can input their own. RooFit is also capable of analytic convolution of specific functions.

Unlike other languages, mathematical objects and operations are represented by a separate object, a RooFit class. This allows for easy, yet robust code writing.

4.2.3 Minuit

The standard utility in particle physics data fitting is the Minuit software code. It is called by ROOT and RooFit when minimization and uncertainty estimation are needed. It has three components that operate on the input likelihood: MIGRAD searches for the minima, HESSE calculates the covariance matrix and MINOS calculates the uncertainty interval.

4.3 Data selection

The analysis presented here uses LHC proton-proton collision data at centre-of-mass energy $\sqrt{s} = 8$ TeV collected by the ATLAS detector in 2012. The integrated luminosity during the data acquisition reached $\int \mathcal{L}\,dt = 20.3$ fb^{-1}. Data were accepted when both systems were operating correctly and LHC beams were stable, passing the ATLAS ready flag.

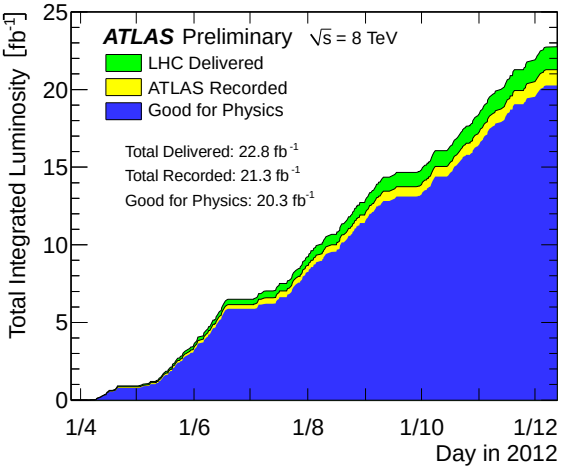

Fig. 4.1: Cumulative luminosity versus time delivered to LHC (green), recorded by ATLAS (yellow), and certified to be good quality data (blue). [9]

4.3.1 Trigger system

Due to overwhelming influx of collision data, certain techniques are employed to reduce the amount, yet keep the measurement relevant.The average event rate is 40 MHz at nominal conditions, which amounts to 10^9 collisions per second. Technical limitations allow only about 10^2 collisions per second to be recorded.

The rejection of events is done by the ATLAS trigger systems. The trigger systems are divided into three levels, the hardware-based Level 1 (L1) and software-based High Level Trigger (HLT) consisting of Level 2 (L2) and Event Filter (EF).

- The L1 trigger is the first one to pass and also provides approximate (θ, ϕ) information. It reduces the event rate down to 75 kHz in less than 2.5 μs. It targets regions of interests located in calorimeters and MS to record potential occurrence of leptons or hadrons with high p_{T}.
- The L2 trigger accepts the L1 information and reconstructs the track in the regions of interest using computationally fast algorithms. Event rate is further reduced to 1 kHz in less than 10 ms.
- The EF trigger finally cuts down the rate to 10^2 Hz with latency of 1 s. It uses the full detector information to perform an online reconstruction of the whole event. 'Raw' data are then saved for further offline reconstruction.

The output is reconstructed by the Athena framework, which is offline software framework used in ATLAS for optimization of the data, and saved for offline work, with a size of 100 kB per event – that is approximately 10 times less compared to the raw data. It produces an event representation that is suitable for analysis, saved in the Analysis Object Data (AOD) file in the form of n-tuples. ROOT is set to read these files using the POOL persistency framework. [16]

4.3.2 Muon reconstruction

In B-physics, muon triggers are of main importance, because B_s meson candidates are reconstructed from the $J/\psi \to \mu^+\mu^-$ decay. The L1 trigger is based on RPC and TGC muon detectors. The trigger is fired in case of coincidence of hits in chamber layers. The L2 trigger then reconstructs the track using information from MDT, comparing it with the ID track. The Level 1 trigger `L1_2MU4` is mainly used. Other triggers were used for a different combinations of muon p_{T}.

Muons leave a clear signature in the subdetectors. Those identified by both MS and ID are referred to as combined and they are well measured. Muons identified by ID only and extrapolated to the MS are called segment-tagged. Muons can be also identified only using MS (such muons are referred to as standalone) and extrapolated to the collision region, or using calorimeters and ID in combination, but they are measured less precisely.

4.3.3 Selection criteria

The occurrence of more than one pp interaction in one event is referred to as pile-up. This produces a large QCD background from which the main signal has to be extracted. A necessary procedure is to find the primary vertex (PV), i.e. the collision point containing the highest sum of p_{T} of the tracks. Tracks coming from the PV are then fitted to the detector hits using χ^2 distribution. Tracks with low goodness of the fit are rejected. Sometimes, χ^2 with reduced degrees of freedom is used (χ^2/d.o.f.).

Candidates for $J/\psi \to \mu^+\mu^-$ decay are selected based on the following selection criteria:

- oppositely charged muons pairs consisting of segment-tagged and combined muons with $p_{\mathrm{T}} > 4$ GeV,
- reconstructed PV from at least four ID tracks with the requirement $\chi^2/\mathrm{d.o.f.} < 10$,
- di-muon invariant mass must fall into selected intervals given η range:
  - $|\eta| < 1.05$ for both muons $\implies m_{\mu\mu} \in (2.959, 3.229)$ GeV,
  - $|\eta| < 1.05$ for one muon and $|\eta| \in (1.05, 2.50)$ for the other muon $\implies m_{\mu\mu} \in (2.913, 3.273)$ GeV,
  - $|\eta| \in (1.05, 2.50)$ for both muons $\implies m_{\mu\mu} \in (2.852, 3.332)$ GeV.

Candidates for $\phi \to K^+K^-$ decay are reconstructed from the oppositely charged tracks that are not identified as muons:

- $p_{\mathrm{T}} > 1$ GeV for K^+K^- candidate, with tracks in $|\eta| < 2.5$,
- the quadruplet of tracks must hit ID (specifically, the SSD) four times,
- reconstructed PV from at least four ID tracks with the requirement $\chi^2/\mathrm{d.o.f.} < 3$,
- K^+K^- invariant mass must fall into the interval $(1.0085, 1.0305)$ GeV.

The B_s candidate is then reconstructed from $B_s \to J/\psi(\mu^+\mu^-)\phi(K^+K^-)$ decay, by fitting the tracks for each K^+K^- and $\mu^+\mu^-$ combination and constraining the $m_{\mu\mu}$ to the PDG average J/ψ mass [17]. This leads to the total number of 5385515 B_s candidates within the selected mass range $m(B_s) \in (5150, 5650)$ GeV.

4.3.4 Proper decay time

The proper decay time $\tau(B_s)$ is defined as

$$\tau = \frac{L_{xy} m_{\mathrm{PDG}}(B_s)}{p_{\mathrm{T}}(B_s)}, \tag{4.14}$$

where $m_{\mathrm{PDG}}(B_s)$ is fixed to the PDG average mass of a B_s meson [17] and L_{xy} the transverse decay length (the transverse displacement of B_s decay vertex to the primary vertex, which is projected onto the B_s transverse momentum $p_{\mathrm{T}}(B_s)$. The proper decay time of the B_s meson will be commonly referred to as lifetime.

4.3.5 Uncertainties

Mass and proper decay time uncertainties σ_{m_i} and σ_{τ_i} were calculated event-by-event from the covariance matrix that is associated with the four-track vertex χ^2 fit. These errors are called per-candidate as they differ for each data point. Events with $\sigma_{m_i} > 160$ MeV and $\sigma_{\tau_i} > 0.3$ ps were removed, reducing the number of candidates by 7 %.

Chapter 5

Results

5.1 Complete model

Two parameters are recovered from the $B_s \to J/\psi(\mu^+\mu^-)\phi(K^+K^-)$ decay as the aim of this work – the reconstructed mass of the B_s meson $m(B_s)$, and its lifetime $\tau(B_s)$. These values are extracted from the two-dimensional unbinned maximum likelihood fit on the selected events, with the mass and lifetime being fitted simultaneously.

The complete likelihood function takes the form of

$$L = \prod_{i=1}^{N} \{f \cdot M_{\text{sig}} T_{\text{sig}} + (1-f) \cdot M_{\text{bkg}} T_{\text{bkg}}\}, \tag{5.1}$$

where the parameter dependence has been hidden for simplicity. The N is the number of events, f denotes the fraction of the signal candidates, M_{sig} and M_{bkg} the mass model components and T_{sig} and T_{bkg} the time model components. The total signal is calculated as a simple product of the signal components $M_{\text{sig}}T_{\text{sig}}$, as they are independent measurements, same with the total background. The following sections will describe the construction of the PDFs in the complete model.

5.2 Mass model

The mass PDF for a given event i operates with the data point m_i and its corresponding error σ_{m_i}. Mass will be fitted in the range from $m_{\text{min}} = 5150$ MeV to $m_{\text{max}} = 5650$ MeV.

The signal component $M_{\text{sig}}(m_i, \sigma_{m_i})$ is presumed to be Gaussian (4.9) with mean value $m(B_s)$ and width $S_m \cdot \sigma_{m_i}$ given as a product of mass uncertainty σ_{m_i} with a scale factor S_m.

$$M_{\text{sig}}(m_i|\sigma_{m_i}) = \frac{1}{S_m \cdot \sigma_{m_i}\sqrt{2\pi}} \exp\left\{-\frac{(m_i - m(B_s))^2}{2(S_m \cdot \sigma_{m_i})^2}\right\}. \tag{5.2}$$

Scale factor is a free parameter that accounts for the slight discrepancy between the detector resolution and calculated per-candidate errors. In an ideal case, it should be equal to one.

The background component $M_{\text{bkg}}(m_i)$ consists of a sum of a constant term with an exponential function:

$$M_{\text{bkg}}(m_i) = a + (1-a)\mathrm{e}^{b \cdot m_i}, \tag{5.3}$$

where a and b are arbitrary parameters.

Take note that the background component does not contain the per-candidate error but the signal component does. In Section 4.1.3, the correction to the likelihood with variable resolution was derived. Adding the necessary Punzi term into Eq. (5.2), we obtain

$$M_{\text{sig}}(m_i, \sigma_{m_i}) = M_{\text{sig}}(m_i|\sigma_{m_i}) \cdot M_{\text{sig}}(\sigma_{m_i}). \tag{5.4}$$

The Punzi term $M_{\text{sig}}(\sigma_{m_i})$ describes the distribution of the signal mass uncertainty. However, this distribution is hidden in the mass uncertainty data, as they contain errors for both signal and background. A method of extracting $M_{\text{sig}}(\sigma_{m_i})$, using so-called data-driven background estimation, is proposed in the following section.

5.2.1 Mass uncertainty

As a first step, a cut is applied to the whole dataset, removing the mass signal portion and associated mass uncertainties. This new dataset contains only the sideband regions. Sideband thresholds have been set at $m_{\text{left}} = 5317$ MeV and $m_{\text{right}} = 5417$ MeV, mass data points now range from $m_i \in (m_{\text{min}}, m_{\text{left}}) \cup (m_{\text{right}}, m_{\text{max}})$.

In the sideband regions, mass uncertainty data points σ_{m_i} are then fitted with an appropriate function. The Landau distribution was chosen empirically for its high resemblance to the obtained data points. It is parametrized by most probable value μ_L, and a scale parameter σ_L. The resulting PDF is shown on Fig. 5.2 and serves as the distribution of total mass uncertainty in the sideband regions.

It is assumed that the total mass uncertainty PDF $M(\sigma_{m_i})$ can be decomposed into two components – the background $M_{\text{bkg}}(\sigma_{m_i})$ and the signal part $M_{\text{sig}}(\sigma_{m_i})$ (that is sought), both being Landau distributions with similar shape (i.e. having the same parameters):

$$M(\sigma_{m_i}) = sM_{\text{sig}}(\sigma_{m_i}) + (1-s)M_{\text{bkg}}(\sigma_{m_i}), \tag{5.5}$$

The two Landau PDFs are bound together with a fraction s that represents the ratio of the signal to background components of mass data. An auxiliary simple mass fit (in the whole mass range) has to be performed to quickly obtain this fraction.

The auxiliary fit is performed using unbinned maximum likelihood with constant resolution.[1] To obtain the signal fraction s as precisely as possible, signal PDF has been chosen as a sum of two general Gaussians (4.9) with the

[1] Binned likelihood can be used instead to reduce computational time.

same mean m_B and different (but constant) widths σ_1, σ_2. The background is chosen to be the same as Eq. (5.3). The auxiliary PDF is given by

$$M_{\text{aux}}(m_i) = s\,[G(m_i; m_B, \sigma_1) + (1-g)G(m_i; m_B, \sigma_2)] + \\ + (1-s)M_{\text{bkg}}(m_i), \tag{5.6}$$

where g represents the relative fraction of the two Gaussians. The first Gaussian represents the normal distribution of the invariant B_s mass. The addition of the second Gaussian can be attributed to the imprecision of the detector resolution. The auxiliary fit is shown on Fig. 5.1.

Once the fraction s is retrieved, it can be plugged into Eq. (5.5) as a fixed constant. RooFit will automatically distribute the Landau PDF $M(\sigma_{m_i})$ into the PDFs describing the background and signal component of the mass uncertainty, as shown on Fig. 5.3. The signal component $M_{\text{bkg}}(\sigma_{m_i})$ is the desired Punzi term for Eq. (5.4), the background component $M_{\text{bkg}}(\sigma_{m_i})$ is discarded as it is not needed, and the fraction s is kept for the time Punzi terms.

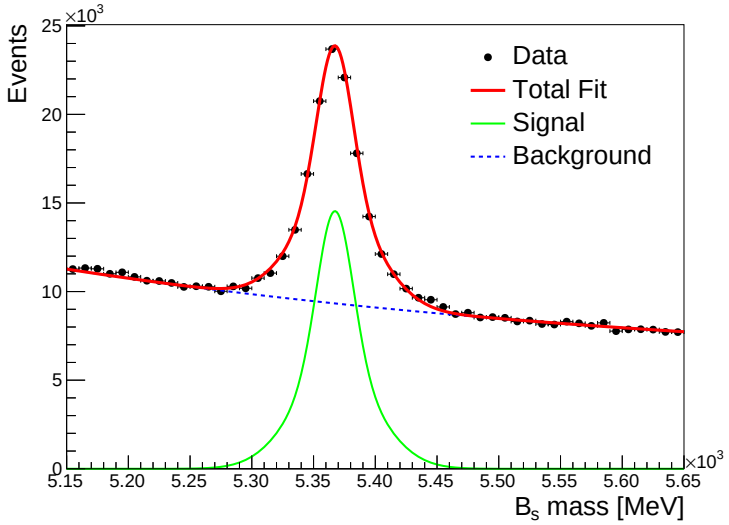

Fig. 5.1: Auxiliary double-gauss fit of the invariant B_s meson mass with signal (green) and background (blue) components.

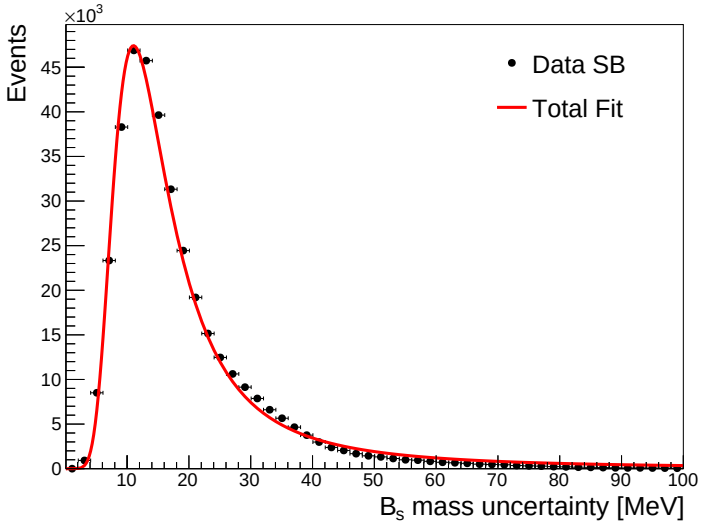

Fig. 5.2: Distribution of the mass uncertainty in the sideband regions.

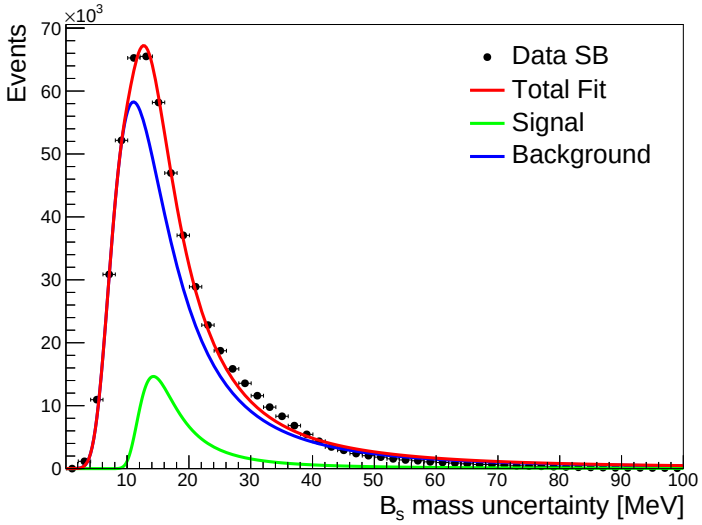

Fig. 5.3: Distribution of the mass uncertainty in the sideband regions (red), with the background (blue) and signal (green) components.

5.3 Time model

The lifetime PDF for a given event i operates with the data point τ_i representing the measured lifetime, and with its corresponding error σ_{τ_i}. The lifetime is fitted in the interval from $\tau_{\min} = -1.0$ ps to $\tau_{\max} = 2.5$ ps. At first, PDFs will be constructed and the Punzi term correction will be added later.

The resolution function is the Gaussian distribution (4.9) as a function of the difference $\tau - \tau_i$, with the following properties: centred at 0, with variable width given as the product of time uncertainty σ_{τ_i} with a scale factor S_τ,

$$G(\tau - \tau_i; 0, \sigma_{\tau_i}) = R(\tau - \tau_i, \sigma_{\tau_i}) = \frac{1}{S_\tau \cdot \sigma_{\tau_i}\sqrt{2\pi}} \exp\left\{-\frac{(\tau - \tau_i)^2}{2(S_\tau \cdot \sigma_{\tau_i})^2}\right\}. \quad (5.7)$$

The scale factor S_τ serves the same purpose as in Eq. (5.2). The signal component $T_{\text{sig}}(\tau_i|\sigma_{\tau_i})$ is modelled as a convolution of the exponential decay function defined for $\tau > 0$ with the time resolution function:

$$T_{\text{sig}}(\tau_i|\sigma_{\tau_i}) = \left[\frac{1}{\tau(B_s)} \exp\left\{-\frac{\tau}{\tau(B_s)}\right\}\right] \otimes R(\tau - \tau_i, \sigma_{\tau_i}). \quad (5.8)$$

The complete signal PDF with τ_i and σ_{τ_i} dependence is obtained by adding the Punzi term representing the signal component of the time uncertainty $T_{\text{sig}}(\sigma_{\tau_i})$:

$$T_{\text{sig}}(\tau_i, \sigma_{\tau_i}) = T_{\text{sig}}(\tau_i|\sigma_{\tau_i}) \cdot T_{\text{sig}}(\sigma_{\tau_i}). \quad (5.9)$$

The acquisition of this term is described in Section 5.3.1.

Two components contribute to the background PDF. The first component is symmetric and describes the prompt J/ψ production:

$$T_p(\tau_i|\sigma_{\tau_i}) = \left[p\delta(\tau) + \frac{1-p}{2\tau_3} \exp\left\{-\frac{|\tau|}{\tau_3}\right\}\right] \otimes R(\tau - \tau_i, \sigma_{\tau_i}), \quad (5.10)$$

where p is the relative fraction between the two components. The exponential function is symmetric with respect to 0 and for both negative and positive decay times it assumes the same decay time τ_3. The negative decay times are attributed to events with poor vertex resolution. The $\delta(\tau)$ is the Dirac delta distribution, which is formally treated as a PDF as well. It acts as the identity element when convolved with any function. This symmetric background contributes the most to the measured data and produces a dominant peak.

Punzi terms representing the background component of the time uncertainty $T_{\text{bkg}}(\sigma_{\tau_i})$ have to be added for both terms separately:

$$\begin{aligned} T_p(\tau_i, \sigma_{\tau_i}) = {} & pR(-\tau, \sigma_{\tau_i}) \cdot T_{\text{bkg}}(\sigma_{\tau_i}) + \\ & + \frac{1-p}{2\tau_3}\left[\exp\left\{-\frac{|\tau|}{\tau_3}\right\} \otimes R(\tau - \tau_i, \sigma_{\tau_i})\right] \cdot T_{\text{bkg}}(\sigma_{\tau_i}), \end{aligned} \quad (5.11)$$

where the delta function was convolved with the resolution function to simplify the expression.

The second component is interpreted as the non-prompt J/ψ production and is given by

$$T_{np}(\tau_i|\sigma_{\tau_i}) = \left[\frac{n}{\tau_1}\exp\left\{-\frac{\tau}{\tau_1}\right\} + \frac{1-n}{\tau_2}\exp\left\{-\frac{\tau}{\tau_2}\right\}\right] \otimes R(\tau, \sigma_{\tau_i}), \tag{5.12}$$

where n yields the relative fraction between the two components. Note that the exponential distributions are not symmetric. The τ_2 and τ_1 represent different lifetimes of the non-prompt J/ψ production: the fast corresponding to misreconstructed J/ψ , and slow corresponding to partially reconstructed J/ψ .

Punzi terms representing the background component of the time uncertainty $T_{\text{bkg}}(\sigma_{\tau_i})$ are again added separately for each term:

$$\begin{aligned} T_{np}(\tau_i, \sigma_{\tau_i}) = &\frac{n}{\tau_1}\left[\exp\left\{-\frac{\tau}{\tau_1}\right\} \otimes R(\tau, \sigma_{\tau_i})\right] \cdot T_{\text{bkg}}(\sigma_{\tau_i}) + \\ &+ \frac{1-n}{\tau_2}\left[\exp\left\{-\frac{\tau}{\tau_2}\right\} \otimes R(\tau, \sigma_{\tau_i})\right] \cdot T_{\text{bkg}}(\sigma_{\tau_i}). \end{aligned} \tag{5.13}$$

Having both background components complete, one can obtain the total time background PDF as their composition:

$$T_{\text{bkg}}(\tau_i, \sigma_{\tau_i}) = t_{bkg}T_p(\tau_i, \sigma_{\tau_i}) + (1 - t_{bkg})T_{np}(\tau_i, \sigma_{\tau_i}), \tag{5.14}$$

where, as expected, the t_{bkg} represents the relative fraction between the prompt and non-prompt components. Note that for the complete time model, we will need both signal $T_{\text{sig}}(\sigma_{\tau_i})$ and background $T_{\text{bkg}}(\sigma_{\tau_i})$ uncertainty components.

5.3.1 Time uncertainty

The Punzi terms $T_{\text{sig}}(\sigma_{\tau_i})$ and $T_{\text{bkg}}(\sigma_{\tau_i})$ will be obtained using the same method described in Section 5.2.1. The lifetime errors σ_{τ_i} are fitted in the region where mass data fall into the sideband regions.

The log-normal distribution assumes that the logarithm of the uncertainty σ_{τ_i} is normally distributed. Here, it was empirically chosen as the PDF of the total time uncertainty, for its high resemblance to data. It is defined as

$$T(\sigma_{\tau_i}) = \frac{1}{\sigma\sqrt{2\pi}}\frac{1}{\sigma_{\tau_i}}\exp\left\{-\frac{(\log\sigma_{\tau_i} - \mu)^2}{2\sigma^2}\right\}, \tag{5.15}$$

where μ is the location parameter and σ the shape factor. The resulting fit is shown on Fig. 5.4, where logarithmic scale was used for convenience.

It is assumed that it be decomposed into the background T_{bkg} and signal T_{sig} components described by PDFs of similar shape (i.e. parameters):

$$T(\sigma_{\tau_i}) = sT_{\text{sig}}(\sigma_{\tau_i}) + (1 - s)T_{\text{bkg}}(\sigma_{\tau_i}). \tag{5.16}$$

The fraction s is read from the already performed auxiliary fit in Eq. (5.6). The resulting PDFs are shown on Fig. 5.5.

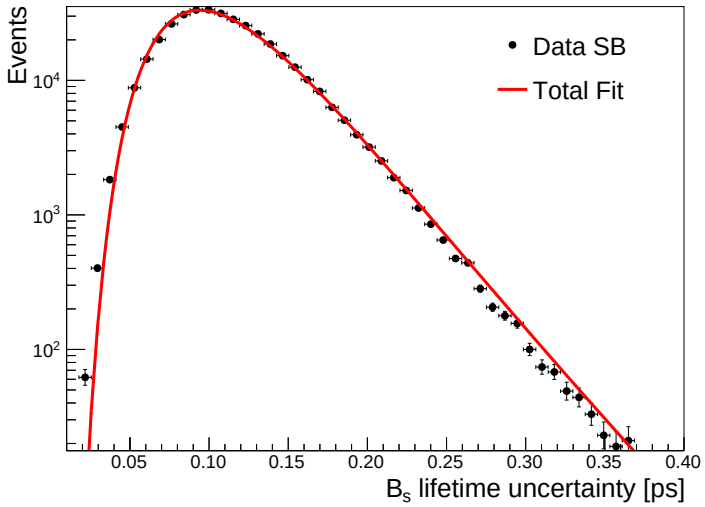

Fig. 5.4: Distribution of the lifetime uncertainty in the mass sideband regions.

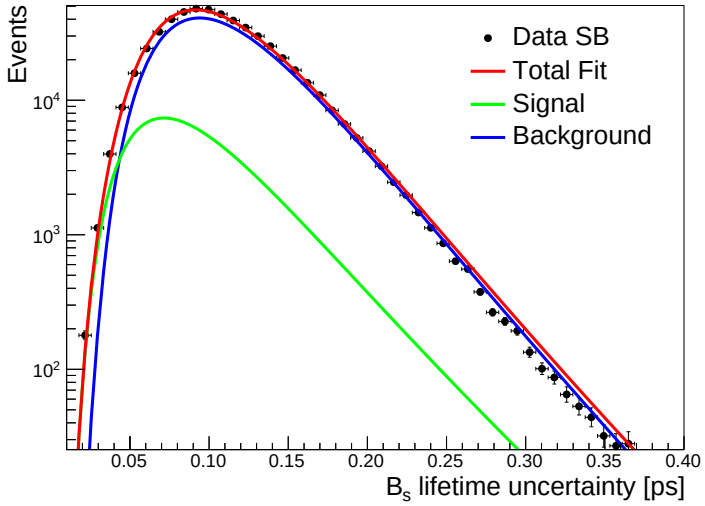

Fig. 5.5: Distribution of the lifetime uncertainty in the sideband regions (red), with the background (blue) and signal (green) components.

5.4 Fit results

The result of the mass and lifetime simultaneous fit using the likelihood given by Eq. (5.1) is projected onto the mass and lifetime axes on Fig. 5.6 and Fig. 5.7. All errors presented in my own analysis are statistical only. Values will be compared to the world average values for B_s meson, calculated from the $B_s \to J/\psi\phi$ decay channel [17]. These reference values will be simply referred to as PDG values and their presented errors will be statistical and systematic combined. For another comparison, values from the ATLAS 2011 study [10] are included as well.

The B_s mass determined from the fit is $m(B_s) = 5366.70 \pm 0.09$ MeV. This value is in very good agreement with world average PDG value for the $m_{\mathrm{PDG}}(B_s) = 5366.7 \pm 0.4$ MeV. The total fit curve slightly underestimates the data, especially at the peak and the region where $5.40 < m_i < 5.45$ MeV. A possible correction would be to add a second background which would account for the contamination of events $B_d \to J/\psi K^{*0}$ that were misreconstructed as $B_s \to J/\psi\phi$.

For the B_s lifetime, fit returns a value of $\tau(B_s) = 1.545 \pm 0.017$ ps. Compared to the average PDG value $\tau_{\mathrm{PDG}}(B_s) = 1.486 \pm 0.018$ ps, the fitted lifetime is noticeably higher. This can be caused by variety of reasons, one of which may be the mentioned B_d decay. Including this term might shift the lifetime slightly backwards, as wanted. Fit could be also improved by adding another background component, or imposing additional selection criteria. The total fit curve replicates the likeness of the data very well in the for positive lifetimes, for $\tau < -0.5$ ps there is a minor underestimation, which is not of physical interest.

The scale factors for mass S_m and time S_τ distributions were fitted to the following values: $S_m = 1.202 \pm 0.005$ and $S_\tau = 1.018 \pm 0.03$. Note that in both cases, scale factor is higher than one, i.e. the detector slightly underestimates the mass and lifetime uncertainties.

Note that the value from the simple auxiliary fit is $m_B = 5367.4 \pm 0.1$ MeV, showing that the simple fit would not be precise enough to determine the B_s mass

The key parameters extracted from the fit with comparison to PDG and ATLAS 2011 values are summarized in the Table 5.1. The time error is rounded to two significant digits on purpose. The table of all fit parameters can be found in the Appendix B.

measured quantity	this analysis	PDG value	ATLAS 2011
$m(B_s)$ [MeV]	5366.70 ± 0.09	5366.7 ± 0.4	5363.7 ± 1.2
$\tau(B_s)$ [ps]	1.545 ± 0.017	1.486 ± 0.018	1.41 ± 0.08

Table 5.1: Main results comparison.

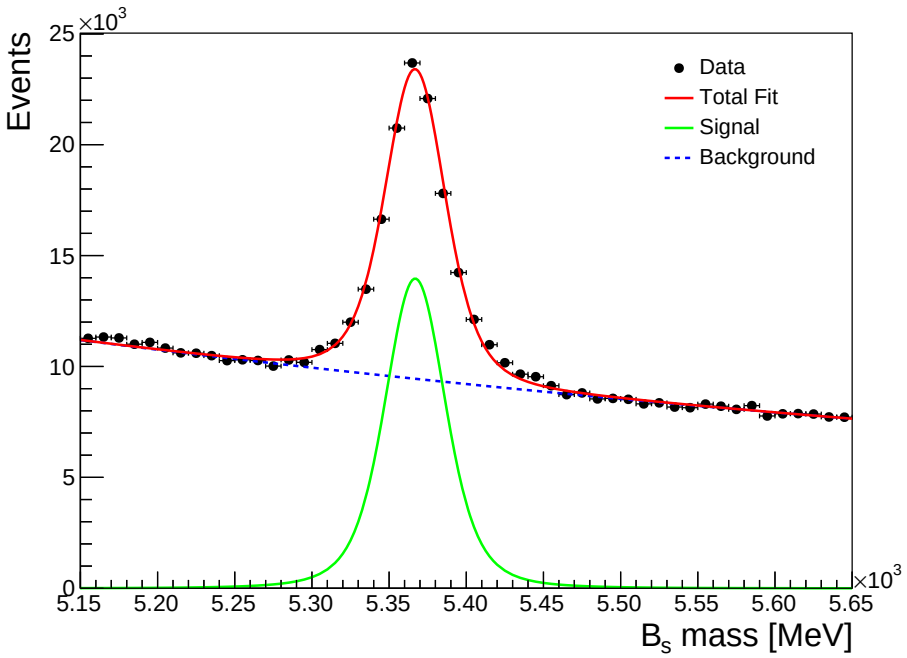

Fig. 5.6: Distribution of the B_s invariant mass (red), with the background (blue) and signal (green) components.

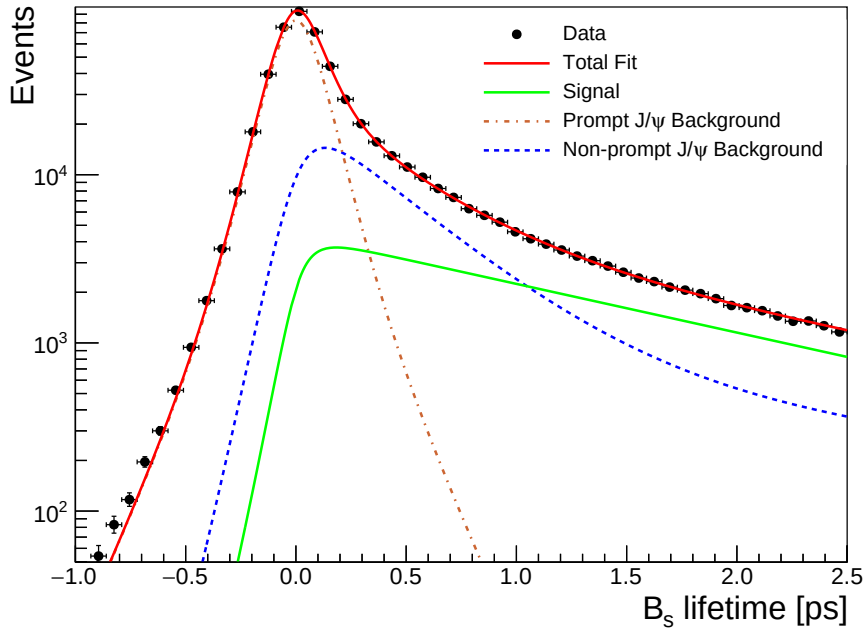

Fig. 5.7: Distribution of the B_s lifetime (red), with the signal (green), prompt J/ψ background (brown) and non-prompt J/ψ (blue) components.

Chapter 6

Conclusion

Aim of this thesis was to study properties of the B_s meson, namely its mass and lifetime. The B_s meson is particularly interesting for its relatively long lifetime and high invariant mass, but mostly for its CP violation related parameters. These were not studied in this thesis, but they are a possible continuation of this work.

The B_s mesons observed in the $B_s \to J/\psi(\mu^+\mu^-)\phi(K^+K^-)$ decay channel were studied. Data used in this analysis were measured and collected in 2012 by ATLAS experiment at the LHC from proton-proton collisions at the centre-of-mass energy of $\sqrt{s} = 8$ TeV with integrated luminosity of 20.3 fb^{-1}.

In order to set the theoretical background, in the first chapter presented a brief overview of several theoretical concepts – mainly the particle content of the Standard Model, with the establishment of beauty mesons. The following chapter characterised the ATLAS experiment, at which the data measurement took place, and necessary variables associated with collider physics.

Third chapter was devoted to B-physics with emphasis on the CP violation. In the fourth chapter, the unbinned maximum likelihood fit was introduced as the means to determine the B_s mass and lifetime from the data. The chapter concluded with selection criteria. In the final chapter, results of the analysis were presented.

The unbinned maximum likelihood fit with variable resolutions was performed successfully and yielded the values of B_s mass and lifetime. Compared to the world average values, the fitted B_s mass is in agreement but a minor deviation of fitted B_s lifetime from the world average value was observed.

Further studies will be based on the skills gained during this thesis, particularly programming in C++, working with ROOT/RooFit and unbinned maximum likelihood fitting. As the next step, angular distributions can be incorporated in the fit, flavour tagging likewise. More complicated fit will allow us to extract the parameters related to the CP violation.

Appendix A
Conventions

In the course of this thesis, natural units are assumed, i.e. the reduced Planck constant and the speed of light are set to one, $\hbar = c = 1$. As a consequence, mass, momentum and energy have same dimensionalities. The following relations are used for conversion from SI to the natural unit system:

$$\begin{aligned} 1\,\mathrm{GeV} &= 1.8 \cdot 10^{-27}\,\mathrm{kg}, \\ 1\,\mathrm{GeV}^{-1} &= 0.197 \cdot 10^{-15}\,\mathrm{m}, \\ 1\,\mathrm{GeV}^{-1} &= 6.58 \cdot 10^{-15}\,\mathrm{s}. \end{aligned}$$

In quantum mechanics, the bra-ket notation is very popular. State of a quantum system corresponds to an abstract ket-vector $|\Psi\rangle$, or simply 'ket', in an infinite-dimensional Hilbert space $\mathcal{H}$, i.e. $|\Psi\rangle \in \mathcal{H}$. Bra-vectors $\langle\Phi|$, or 'bras', are obtained by applying hermitian conjugation, i.e. $\langle\Phi| = |\Phi\rangle^\dagger$. Operators on the Hilbert space are denoted with a hat (e.g. helicity $\hat{\lambda}$), in addition, vector operators are bold-faced (e.g. spin $\hat{\mathbf{S}}$).

To recover a quantum state wavefunction Ψ in the position basis, one must multiply the ket $|\Psi\rangle$ with bra $\langle x|$,

$$\langle x|\Psi\rangle = \Psi(x), \tag{A.1}$$

where ket $|x\rangle = \langle x|^\dagger$ denotes the eigenvector of the position operator $\hat{\mathrm{x}}$, i.e. $\hat{\mathrm{x}}\,|x\rangle = x\,|x\rangle$. The term $\langle x|\Psi\rangle$ is de facto a scalar product of the two abstract vectors. In three-dimensional Euclidean vector space, the scalar product of two column vectors $\boldsymbol{u} = (u_1, u_2, u_3)^\mathrm{T}$, $\boldsymbol{v} = (v_1, v_2, v_3)^\mathrm{T}$ is evaluated as

$$\boldsymbol{u} \cdot \boldsymbol{v} = u_1 v_1 + u_2 v_2 + u_3 v_3. \tag{A.2}$$

Euclidean norm of a vector $\boldsymbol{v}$ given above is calculated as

$$\|\boldsymbol{v}\| = \sqrt{\boldsymbol{v} \cdot \boldsymbol{v}} = \sqrt{(v_1)^2 + (v_2)^2 + (v_3)^2}. \tag{A.3}$$

Minkowski norm[1] of a 4-vector $V^\nu = (V^0, v^1, v^2, v^3)^\mathrm{T} = (V^0, \boldsymbol{v})^\mathrm{T}$ is given by

$$V^\nu V_\nu = \eta_{\nu\mu} V^\nu V^\mu = (V^0)^2 - \|\boldsymbol{v}\|^2, \tag{A.4}$$

where $\eta_{\nu\mu} = \mathrm{diag}(1, -1, -1, -1)$ is the Minkowski metric given as usual in particle physics, and summation over repeated indices is implied.

[1] Technically speaking, it is a square of the Minkowski norm.

Appendix B

Fit parameters

The dimensionalities are not shown to conserve space, but they can be easily derived from the corresponding PDFs.

parameter name	symbol	fit value	± (stat.err.)
B_s mass	$m(B_s)$	5366.70	0.09
B_s lifetime	$\tau(B_s)$	1.545	0.017
mass scale factor	S_m	1.202	0.005
lifetime scale factor	S_τ	1.018	0.003
exponential slope	b	$-1.20 \cdot 10^{-3}$	$0.09 \cdot 10^{-3}$
linear part of background	a	$6.5603 \cdot 10^{-1}$	$0.5 \cdot 10^{-1}$
signal fraction	f	$137.5 \cdot 10^{-3}$	$0.7 \cdot 10^{-3}$
time background fraction	t_{bkg}	$680 \cdot 10^{-3}$	$1 \cdot 10^{-3}$
fraction between non-prompt bkg	n	$1.5 \cdot 10^{-1}$	$0.1 \cdot 10^{-1}$
fraction between prompt bkg	p	$893 \cdot 10^{-3}$	$4 \cdot 10^{-3}$
non-prompt lifetime 1	τ_1	2.2	0.3
non-prompt lifetime 2	τ_2	$376 \cdot 10^{-3}$	$6 \cdot 10^{-3}$
prompt lifetime	τ_3	$153 \cdot 10^{-3}$	$3 \cdot 10^{-3}$

Table B.1: Values extracted from the complete fit.

parameter name	symbol	fit value	± (stat.err.)
exponential slope	b	$-1.8 \cdot 10^{-3}$	$0.7 \cdot 10^{-3}$
linear part of background	a	$4.2 \cdot 10^{-1}$	$0.8 \cdot 10^{-1}$
fraction between two Gaussians	g	$4.1 \cdot 10^{-1}$	$0.3 \cdot 10^{-1}$
mass signal fraction	s	$144 \cdot 10^{-3}$	$2 \cdot 10^{-3}$
mean B_s mass	m_B	5367.4	0.1
sigma of Gaussian 1	σ_1	14.2	0.5
sigma of Gaussian 2	σ_2	32	1

Table B.2: Values extracted from the auxiliary mass fit.

parameter name	symbol	fit value	± (stat.err.)
Landau most probable value	μ_L	14.70	0.05
Landau scale parameter	σ_L	1.96	0.02
Log-normal location	μ	$85.37 \cdot 10^{-3}$	$0.03 \cdot 10^{-3}$
Log-normal shape factor	σ	1.523	0.003

Table B.3: Values extracted from the Punzi term fits.

Appendix C

Bibliography

[1] Wikimedia Commons, "Standard Model of Elementary Particles," 2015, accessed 30-June-2015. [Online]. Available: https://commons.wikimedia.org/wiki/File:Standard_Model_of_Elementary_Particles.svg

[2] C. Hull, "Introduction to particle physics," 2009, accessed 20-June-2015. [Online]. Available: https://workspace.imperial.ac.uk/theoreticalphysics/Public/MSc/PartSymm/ParticlePhysicsNotes.pdf

[3] C. Amsler, "Mesons and baryons in the quark model," 2014, accessed 20-June-2015. [Online]. Available: http://www.lhep.unibe.ch/schumann/docs/amsler_baryonsmesons.pdf

[4] CERN, "The CERN accelerator complex," 2015, accessed 5-May-2015. [Online]. Available: https://espace.cern.ch/acc-tec-sector/default.aspx

[5] G. Aad *et al.*, "The ATLAS Experiment at the CERN Large Hadron Collider," *JINST*, vol. 3, p. S08003, 2008.

[6] J. Pequenao and P. Schaffner, "An computer generated image representing how ATLAS detects particles," Jan 2013. [Online]. Available: https://cds.cern.ch/record/1505342

[7] A. J. Bevan *et al.*, "The Physics of the B Factories," *Eur. Phys. J.*, vol. C74, p. 3026, 2014.

[8] S. Stone and L. Zhang, "Use of $B \to J/\psi f_0$ decays to discern the $q\bar{q}$ or tetraquark nature of scalar mesons," *Phys.Rev.Lett.*, vol. 111, no. 6, p. 062001, 2013.

[9] ATLAS collaboration, "LuminosityPublicResults," 2015, accessed 10-May-2015. [Online]. Available: https://twiki.cern.ch/twiki/bin/view/AtlasPublic/LuminosityPublicResults

[10] "Measurement of the B_0 and B_s^0 lifetimes in the decay modes $B_0 \to J/\psi K^{*0}$ and $B_s^0 \to J/\psi\phi$ in ATLAS," 2011.

[11] R. Aaij *et al.*, "Observation of the resonant character of the $Z(4430)^-$ state," *Phys. Rev. Lett.*, vol. 112, no. 22, p. 222002, 2014.

[12] ——, "Observation of $J/\psi p$ resonances consistent with pentaquark states in $\Lambda_b^0 \to J/\psi K^- p$ decays," 2015.

[13] M. Kobayashi and T. Maskawa, "CP Violation in the Renormalizable Theory of Weak Interaction," *Prog. Theor. Phys.*, vol. 49, pp. 652–657, 1973.

[14] INSPIRE, "Top cited articles during 2014," 2015, accessed 26-June-2015. [Online]. Available: http://inspirehep.net/info/hep/stats/topcites/2014/annual.html

[15] G. Punzi, "Comments on likelihood fits with variable resolution," *eConf*, vol. C030908, p. WELT002, 2003, [,235(2004)].

[16] W. Bhimji, J. Cranshaw, P. van Gemmeren, D. Malon, R. D. Schaffer, and I. Vukotic, "The ATLAS ROOT-based data formats: recent improvements and performance measurements," CERN. Geneva: CERN, 2012. [Online]. Available: http://cdsweb.cern.ch/record/1448601/files/ATL-SOFT-PROC-2012-020.pdf

[17] K. Olive *et al.*, "Review of particle physics," *Chin.Phys.*, vol. C38, p. 090001, 2014.

[18] J. R. Catmore, "$B_s \to J/\psi\phi$ with LHC-ATLAS : simulations and sensitivity studies."

[19] M. Zeman, "Measurement of the Standard Model W^+W^- production cross-section using the ATLAS experiment on the LHC," Ph.D. dissertation, IRFU, Saclay. [Online]. Available: https://inspirehep.net/record/1381339/files/Thesis-2014-Zeman_2.pdf

[20] D. H. Perkins, *Introduction to high-energy physics; 4th ed.* Cambridge: Cambridge Univ. Press, 2000. [Online]. Available: https://cds.cern.ch/record/396126

[21] G. Aad *et al.*, "Expected Performance of the ATLAS Experiment - Detector, Trigger and Physics," 2009.

[22] "J/ψ Performance of the ATLAS Inner Detector," 2010.

[23] ATLAS Collaboration, "Flavour tagged time dependent angular analysis of the $B_s \to J/\psi\phi$ decay and extraction of $\Delta\Gamma$ and the weak phase ϕ_s in ATLAS," *Phys. Rev. D*, vol. 90, no. CERN-PH-EP-2014-043, p. 052007. 26 p, Jul 2014. [Online]. Available: https://cds.cern.ch/record/1741328

[24] H. Pernegger, "The Pixel Detector of the ATLAS experiment for LHC Run-2," *JINST*, vol. 10, no. 06, p. C06012, 2015.

[25] K. Cranmer, "Practical Statistics for the LHC," in *Proceedings, 2011 European School of High-Energy Physics (ESHEP 2011)*, 2014, pp. 267–308. [Online]. Available: http://inspirehep.net/record/1356277/files/arXiv:1503.07622.pdf

[26] W. Verkerke and D. P. Kirkby, "The RooFit toolkit for data modeling," *eConf*, vol. C0303241, p. MOLT007, 2003, [,186(2003)].

[27] W. Verkerke, "Roofit toolkit for data modeling," 2015. [Online]. Available: http://roofit.sourceforge.net/

[28] R. Cousins., "Probability density functions for positive nuisance parameters." 2010. [Online]. Available: http://www.physics.ucla.edu/~cousins/stats/cousins_lognormal_prior.pdf